The Astrophysical Journal, 971:9 (26pp), 2024 August 10 https://doi.org/10.3847/1538-4357/ad58d3

Rotation and Abundances of the Benchmark Brown Dwarf HD 33632 Ab from Keck/KPIC High-resolution Spectroscopy

Chih-Chun Hsu[1], Jason J. Wang (王劲飞)[1,2], Jerry W. Xuan[3], Jean-Baptiste Ruffio[3,4], Evan Morris[5], Daniel Echeverri[3], Yinzi Xin[3], Joshua Liberman[3,6], Luke Finnerty[7], Katelyn Horstman[3], Ben Sappey[4], Gregory W. Doppmann[8], Dimitri Mawet[3,9], Nemanja Jovanovic[3], Michael P. Fitzgerald[7], Jacques-Robert Delorme[8], J. Kent Wallace[9], Ashley Baker[3], Randall Bartos[9], Geoffrey A. Blake[10], Benjamin Calvin[3,7], Sylvain Cetre[8], Ronald A. López[7], Jacklyn Pezzato[3], Tobias Schofield[3], Andrew Skemer[5], and Ji Wang[11]
[1] Center for Interdisciplinary Exploration and Research in Astrophysics (CIERA), Northwestern University, 1800 Sherman Ave, Evanston, IL 60201, USA; chsu@northwestern.edu
[2] Department of Physics and Astronomy, Northwestern University, 2145 Sheridan Rd, Evanston, IL 60208, USA
[3] Department of Astronomy, California Institute of Technology, Pasadena, CA 91125, USA
[4] Center for Astrophysics and Space Sciences, University of California, San Diego, La Jolla, CA 92093, USA
[5] Department of Astronomy & Astrophysics, University of California, Santa Cruz, CA 95064, USA
[6] James C. Wyant College of Optical Sciences, University of Arizona, Meinel Building 1630 E. University Blvd., Tucson, AZ 85721, USA
[7] Department of Physics & Astronomy, 430 Portola Plaza, University of California, Los Angeles, CA 90095, USA
[8] W. M. Keck Observatory, 65-1120 Mamalahoa Hwy, Kamuela, HI, USA
[9] Jet Propulsion Laboratory, California Institute of Technology, 4800 Oak Grove Dr., Pasadena, CA 91109, USA
[10] Division of Geological & Planetary Sciences, California Institute of Technology, Pasadena, CA 91125, USA
[11] Department of Astronomy, The Ohio State University, 100 W 18th Ave, Columbus, OH 43210, USA
Received 2023 November 9; revised 2024 June 13; accepted 2024 June 14; published 2024 August 1

Abstract

We present the projected rotational velocity and molecular abundances for HD 33632 Ab obtained via Keck Planet Imager and Characterizer (KPIC) high-resolution spectroscopy. HD 33632 Ab is a nearby benchmark brown dwarf companion at a separation of ∼20 au that straddles the L–T transition. Using a forward-modeling framework with on-axis host star spectra, which provides self-consistent substellar atmospheric and retrieval models for HD 33632 Ab, we derive a projected rotational velocity of 53 ± 3 km s^{-1} and carbon monoxide and water mass fractions of $\log \mathrm{CO} = -2.3 \pm 0.3$ and $\log \mathrm{H_2O} = -2.7 \pm 0.2$, respectively. The inferred carbon-to-oxygen ratio ($\mathrm{C/O} = 0.58 \pm 0.14$), molecular abundances, and metallicity ($[\mathrm{C/H}] = 0.0 \pm 0.2$ dex) of HD 33632 Ab are consistent with its host star. Although detectable methane opacities are expected in L–T transition objects, we did not recover methane in our KPIC spectra, partly due to the high $v \sin i$ and to disequilibrium chemistry at the pressures to which we are sensitive. We parameterize the spin as the ratio of rotation to the breakup velocity, and compare HD 33632 Ab to a compilation of >200 very low-mass objects ($M \lesssim 0.1\ M_\odot$) that have spin measurements in the literature. There appears to be no clear trend for the isolated low-mass field objects versus mass, but a tentative trend is identified for low-mass companions and directly imaged exoplanets, similar to previous findings. A larger sample of close-in gas giant exoplanets and brown dwarfs will critically examine our understanding of their formation and evolution through rotation and chemical abundance measurements.

Unified Astronomy Thesaurus concepts: Brown dwarfs (185); L dwarfs (894); Atmospheric composition (2120); High resolution spectroscopy (2096); High angular resolution (2167); Stellar rotation (1629)

1. Introduction

More than 5500 exoplanets have been discovered since the discovery of 51 Peg b, the first exoplanet around a main-sequence star (Mayor & Queloz 1995), with <30 directly imaged (gas giant) exoplanets (e.g., Marois et al. 2008; Macintosh et al. 2015; Franson et al. 2023).[12] In contrast, tens of thousands of brown dwarfs have been found within a kiloparsec of the Sun. Brown dwarfs share similar temperatures and atmospheric properties with gas giant exoplanets (Burrows et al. 1997, 2001; Baraffe et al. 2003), but are more massive and brighter at the same age, allowing us to characterize their atmospheric properties more easily.

Measuring the rotation rates and atmospheric content of brown dwarfs and gas giant exoplanets via molecular spectroscopy enables constraining the theories of their formation and evolution, because the rotation of these low-mass objects imprints their angular momentum evolution. As brown dwarfs evolve into field age (>1 Gyr), they lose little angular momenta, and spin up until their radii contract to $\sim 1\ R_{\mathrm{Jup}}$, with the size governed by electron degeneracy pressure (Zapatero Osorio et al. 2006; Vos et al. 2017; Hsu et al. 2021; Vos et al. 2022). In the planetary-mass regime, objects also spin up and roughly follow angular momentum conservation as they age after disk clearance (Bryan et al. 2020). During their earlier phases, the magnetic fields of low-mass companions can interact with the magnetized circumplanetary disk and release their angular momenta (Batygin 2018). It is predicted that the angular momentum loss is mass dependent because gas giant exoplanets or brown dwarf companions have different levels of magnetic fields, regulated by their masses,

[12] The number of the directly imaged exoplanets is based on Currie et al. (2023) and the NASA Exoplanet Archive.

temperatures, and therefore degrees of ionization (Ginzburg & Chiang 2020). Tentative evidence of an anticorrelation has been found between rotation and companion mass (Bryan et al. 2020; Wang et al. 2021) in a small sample size of <20 low-mass companions.

For chemical abundances, the carbon-to-oxygen (C/O) ratio has been widely used to infer the location of planet formation, as the ice lines of H_2O, CO_2, and CO are different, which lead to different observed (gas-phase) C/O ratios for planets assembled at different semimajor axes in the disk (Öberg et al. 2011; Madhusudhan 2012; Konopacky et al. 2013; Lavie et al. 2017; Mollière et al. 2020; Nowak et al. 2020; Mollière et al. 2022; Hoch et al. 2023; Whiteford et al. 2023; Nasedkin et al. 2024b). Brown dwarf companions, either formed through gravitational core collapse or disk instability, are expected to share the same C/O ratios with their host stars because their formation is star-like (Bate & Bonnell 2005). Detailed characterization of brown dwarf abundances not only facilitates our understanding of star formation at the very low-mass (VLM) end but also serves as an independent calibrator of the methodology used to characterize gas giant exoplanets (e.g., Burningham et al. 2017; Wang et al. 2022; Adams et al. 2023).

However, a major challenge of studying brown dwarfs as exoplanet analogs is the observed degeneracy between age, mass, and bolometric luminosity. Because brown dwarfs are unable to fuse hydrogen and are supported by electron degeneracy pressure (Kumar 1962, 1963), they constantly cool and evolve under hydrostatic equilibrium. A given spectral type, which corresponds to a given range of effective temperatures, could represent either a low-mass star, a brown dwarf, or a very young, hot exoplanet at ∼3000 K (Burrows et al. 2001; Baraffe et al. 2003). One way to break the age degeneracy is through the identification of brown dwarfs in young star clusters or moving groups (Gagné et al. 2017, 2018a, 2018b; Schneider et al. 2023). Another route is through the discovery of brown dwarfs in FGK binary systems because these solar-like stars have independent estimates of age, mass, and metallicity. While wide binary FGK systems with brown dwarf companions have been identified (e.g., Faherty et al. 2021; Zhou et al. 2023), such widely separated companions typically have long orbital periods—meaning that the dynamical masses are not well constrained over a timescale of a few decades. Close companions, on the other hand, provide reliable dynamical masses through direct imaging and absolute and relative astrometry with Gaia (Gaia Collaboration et al. 2016, 2018, 2021, 2023) and Hipparcos (ESA Special Publication 1997; Perryman et al. 1997; van Leeuwen et al. 1997) as they provide better orbital phase coverage.

Thus, close-in, low-mass companions can serve as benchmark objects with independent ages and dynamical masses, but the precise characterization of their rotation and abundances are difficult due to being so close to the bright host star and the high contrasts (5–15 mag) that must be achieved to isolate them. Designed to overcome these challenges, the Keck Planet Imager and Characterizer (KPIC; Mawet et al. 2016, 2017, 2018; Delorme et al. 2021) is a fiber injection unit connecting the Keck/Near-InfraRed SPECtrometer (NIRSPEC; $R \sim 35{,}000$; McLean et al. 1998, 2000; Martin et al. 2018) to the Keck II adaptive optics (AO) system via a single-mode fiber to provide high-resolution K-band spectroscopy at high angular resolution. With its high spectral resolution, rotation and chemical abundances can be reliably measured. Several benchmark brown dwarfs and gas giant exoplanets have been characterized and reported with KPIC, providing robust abundances and rotation, including the HR 8799 cde planets (Wang et al. 2021, 2023), HR 7672B (Wang et al. 2022), and HD 4747 B (Xuan et al. 2022).

HD 33632 Ab is a brown dwarf companion of mass $46 \pm 8\ M_{\rm Jup}$ (Currie et al. 2020) that straddles the L–T transition ($L9.5^{+1.0}_{-3.0}$) around the F8V star HD 33632A at an ∼20 au separation. The system was initially identified by a Gaia/Hipparcos acceleration trend and confirmed with SCExAO/CHARIS and Keck/NIRC2 imaging by Currie et al. (2020). The host star HD 33632A has a field age of 1.0–2.5 Gyr (Currie et al. 2020) and slightly subsolar metallicity ($[{\rm Fe/H}] = -0.15 \pm 0.03$ dex; Rice & Brewer 2020). With an independent age, metallicity (abundances), and dynamical mass, HD 33632 Ab serves as a benchmark brown dwarf to break the observational degeneracy among the population of brown dwarfs and gas giant exoplanets. The system properties are summarized in Table 1.

In this work, we present follow-up Keck/KPIC observations of the HD 33632 Ab system to derive its companion rotation rate, RV, and abundances. Our manuscript is organized as follows. In Section 2 we describe our KPIC observations. In Section 3 we show our detection of CO and H_2O using the cross-correlation method. In Section 4 we forward model our KPIC spectra using self-consistent substellar atmosphere models to derive radial and projected rotational velocities. In Section 5 we employ our retrieval modeling framework to extract the CO and H_2O abundances and validate the nondetection of methane in the KPIC data. In Section 6 we update the orbital solutions of the HD 33632 Ab system using our measured companion RVs and updated astrometry. We compare the rotation of HD 33632 Ab with other low-mass objects to examine if there exists a population-level trend in Section 7. We summarize our findings in Section 8.

2. Observations and Data Reduction

We obtained our high-resolution near-infrared spectra of HD 33632 A and HD 33632 Ab on 2021 September 18 (UT) and 2021 November 20 (UT), using the KPIC (Mawet et al. 2016, 2017, 2018; Delorme et al. 2021). KPIC is an AO system mounted on the Keck II telescope that is optimized for high-resolution spectroscopy and high-contrast coronagraphic imaging, which couples the light using a single-mode fiber injection unit to NIRSPEC ($R \sim 35{,}000$; McLean et al. 1998, 2000; Martin et al. 2018; López et al. 2020) and NIRC2 (van Dam et al. 2006; Wizinowich et al. 2006; Vargas Catalán et al. 2016; Serabyn et al. 2017). The KPIC instrumental design is detailed in Mawet et al. (2017) and Delorme et al. (2021). The "Kband-new" filter on NIRSPEC covers a wavelength range of 1.91–2.55 μm. KPIC has four single-mode fibers (fluoride 6.5/125 μm) to place the science targets, and two fibers were typically used to enable nod subtraction. On 2021 September 18, four spectra of HD 33632 A were observed, each with a 60 s integration time, and nine spectra of HD 33632 Ab were acquired, each with a 600 s integration time. We used fibers 2 and 3. For our calibration data, the M2.5III giant HIP 81497 was observed for wavelength calibration, while the A0 HD 33704 served to obtain the spectral traces and the instrumental response function. On 2021 November 20, 14 spectra of HD 33632 A were observed, each with a 30 s integration time, with 12 spectra of HD 33632 Ab obtained, each with a 600 s integration time. We used fibers 1 and 2. Here, the M0.5III giant HIP 95771 served as the wavelength calibrator, while A1V Omega Aurigae (Zuckerman

Table 1
HD 33632 System Properties

Property (Unit)	Value	Ref.
	HD 33632 A	
R.A. (J2000)	05:13:17.45	(1)
Decl. (J2000)	+37:20:14.32	(1)
μ_α (mas yr^{-1})	-144.922 ± 0.031	(1)
μ_δ (mas yr^{-1})	-136.772 ± 0.022	(1)
Mass ($M_\odot$)	1.1 ± 0.1	(2)
Age (Gyr)	1.0–2.5	(2)
SpT	F8V	(3)
Gaia G	6.351 ± 0.003	(1)
$J_{\rm MKO}$ (mag)	5.43 ± 0.02	(4)
$H_{\rm MKO}$ (mag)	5.193 ± 0.015	(4)
$K_{\rm S,MKO}$ (mag)	5.17 ± 0.02	(4)
π (mas)	37.895 ± 0.026	(1)
distance (pc)	26.388 ± 0.018	(1)
Radial velocity (RV; km s^{-1})	-1.75 ± 0.12	(1)
$v \sin i$ (km s^{-1})	$\lesssim 4$	(5),[a] (6)
[Fe/H]	-0.15 ± 0.03	(6)
[C/H]	-0.13 ± 0.05	(6)
C/O	$0.39^{+0.12}_{-0.09}$	(6), (7)
	HD 33632 Ab	
Mass ($M_{\rm Jup}$)	46 ± 8	(2)
…	37 ± 7	(7)
SpT	$\rm L9.5^{+1.0}_{-3.0}$	(2)
$J_{\rm MKO}$ (mag)	16.91 ± 0.11	(2)
$H_{\rm MKO}$ (mag)	16.00 ± 0.09	(2)
$Ks_{\rm MKO}$ (mag)	15.37 ± 0.09	(2)
$v \sin i$ (km s^{-1})	53 ± 3	(7)
RV (km s^{-1})[b]	-8 ± 3	(7)
[C/H] (dex)	0.0 ± 0.2	(7)
C/O	0.58 ± 0.14	(7)
a (au)	18^{+5}_{-3}	(7)
e	$0.25^{+0.17}_{-0.18}$	(7)
i (deg)	33^{+11}_{-21}	(7)
P (yr)	74^{+34}_{-16}	(7)

Notes.
[a] Note that the measured $v \sin i = 0.44$ km s^{-1} in Rice & Brewer (2020) using the Keck/HIRES data has a resolution limit of ∼4 km s^{-1}.
[b] Barycentric RV measured on MJD 59538.436.
References: (1) Gaia Collaboration et al. (2023), (2) Currie et al. (2020), (3) Gray et al. (2003), (4) Cutri et al. (2003), (5) Nordström et al. (2004);, (6) Rice & Brewer (2020), and (7) this work.

et al. 2011) was observed for spectral order tracing and spectral response. On both nights, NIRSPEC backgrounds with the same integration were also obtained, so that the sky backgrounds could be either removed using another nodding position or the thermal background measured under the same integration time (see below).

The data were reduced using the `KPIC Data Reduction Pipeline`,[13] detailed in Section 3 of Wang et al. (2021). The reduction steps include instrumental thermal background subtraction, trace finding using a telluric standard star (typically A0V stars),[14] standard spatial and spectral rectification and optimal extraction (Horne 1986), and finally wavelength calibration using early M giant star spectra. The wavelength calibration precision of Keck/NIRSPEC spectrograph is typically around 0.1–0.5 km s^{-1}, using Earth absorption lines from telluric standard star spectra (Blake et al. 2010; Burgasser et al. 2016; Hsu et al. 2021; Theissen et al. 2022; Hsu et al. 2023).

We assessed the data quality for each night based on the end-to-end throughput based on the associated M giant spectra using HIP 81497 and HIP 95771, respectively. Using their K-band photometry (0.467 and 0.711 mag, respectively) from Cutri et al. (2003) and effective temperatures (3774 and 3972 K, respectively) from Stassun et al. (2019), the 95th percentile peak throughputs of HIP 81497 on 2021 September 18 and of HIP 95771 on 2021 November 20 are 1.3% (poor KPIC performance) and 2.4% (typical KPIC performance), respectively; the former is the result of more unstable seeing on 2021 September 18 compared to the 2021 November 20 night.[15]

Various subtraction methods for data reduction are used under different circumstances, to maximize the detection of the companion flux and minimize speckling from the host star. The first subtraction method uses the thermal background of the same integration time as the science file. The second subtraction method, nod subtraction, uses a science file of the same integration time from another fiber, similar to the traditional pair subtraction on slit-fed spectroscopy. For our HD 33632 Ab data on 2021 November 20, we found that the nod-subtracted flux on star fiber 1 and background-subtracted flux on star fiber 2 provided the highest S/N, as the speckle flux on fiber 2 caused poor subtraction. For data on the same fiber, the bad pixels were removed using a 3σ clipping outlier rejection, and the resulting statistical uncertainties were then computed. We focus on NIRSPEC orders 33 (2.29–2.34 μm), 32 (2.36–2.41 μm), and 31 (2.43–2.49 μm), in which we could obtain robust wavelength calibrations with sufficient companion fluxes.

3. Cross-correlation Method to Detect Molecules

The cross-correlation method using spectral templates is a powerful tool for detecting possible species in low-mass companions (e.g., Konopacky et al. 2013; Ruffio et al. 2021; Wang et al. 2021; Patapis et al. 2022; Xuan et al. 2022; Mâlin et al. 2023). Specifically, we employed a least-squares cross-correlation function (CCF) to cross-correlate the observed companion flux and incorporate the star flux contribution, tellurics, and instrument response. Our method has been detailed in Wang et al. (2021) and Xuan et al. (2022), so we briefly summarize it here.

We cross-correlate the observed spectra (orders 31–33; 2.29–2.49 μm) using forward-model molecular templates. The forward model includes the companion and star flux contributions. For the companion flux component, we used the molecular templates (CO, H_2O, and CH_4) from the Sonora–Bobcat model sets (Marley et al. 2021; see the justification in Wang et al. 2021). These templates were first multiplied by the telluric absorption and the spectral response function. The specific molecular templates were derived from the cloudless Sonora–Bobcat model set (Marley et al. 2018, 2021) by turning on specific molecular species including carbon monoxide (CO), water (H_2O), methane (CH_4), and carbon monoxide and water

[13] https://github.com/kpicteam/kpic_pipeline
[14] The telluric standard stars are used to identify the trace and derive the spectral response. Our reduced spectra include telluric absorption and will be forward modeled using the observed star and telluric spectra. See Section 4 for details.
[15] The signal-to-noise ratio (S/N), defined as the 99th percentile of observed flux, was ∼13 on 2021 September 18 and ∼20 on 2021 November 20. The companion fluxes have S/Ns of ∼1.8 and ∼3.4, respectively, inferred from our best-fit companion fluxes in Section 4.

($CO + H_2O$). The telluric spectra were directly taken from our observed spectra of Omega Aurigae. The spectral response function, defined as the sensitivity of a given spectral order, was measured by the observed flux (A1V Omega Aurigae) over the expected flux using the telluric spectra, normalized at the 99th percentile flux ratio to reduce the effects from the outlier fluxes. For the theoretical atmospheric model of the telluric spectra, we used `PHOENIX ACES AGSS COND` models (Husser et al. 2013), assuming an effective temperature $T_{\rm eff} = 9400$ K, surface gravity $\log g = 4.0$ cm s^{-2} dex, and solar metallicity, which is consistent with the empirical $T_{\rm eff}$ and $\log g$ relations from Pecaut & Mamajek (2013). For the star flux contribution, we used the observed on-axis star spectra as an empirical template. The cross-correlation signal of the companion flux can then be estimated through the maximum likelihood. We used the least-squares method by optimizing the observed companion spectra and the forward model as a function of RV shift. Interested readers are referred to Wang et al. (2021) for this mathematical formulation. Note that our result might still be biased by imperfect modeling of the star flux contribution (see Section 4 for details).

Our confidence in the detection(s) of molecular species was computed based on the S/N, where the signal of the molecular CCF was first normalized to the baseline using the CCF wings of the last ± 500 km s^{-1}, and then compared with the standard deviation of CCF wings of the same last ± 500 km s^{-1} as the noise. Under this formulation, the CCF S/N could be negative, and using the CCF wings to estimate allows us to quantify the instrument systematics in addition to the background noise. The RV shifts of the CCF range from -1000 to $+1000$ km s^{-1} in steps of 1 km s^{-1}. Figure 1 illustrates the CCFs of HD 33632 Ab (with both stellar and brown dwarf fluxes), compared to the RV of the primary HD 33632 A at the time of observation (-12.65 km s^{-1}), which includes its systematic RV $= -1.75 \pm 0.12$ km s^{-1} (Gaia Collaboration et al. 2023) and its barycentric velocity at the time of the observation ($+10.903$ km s^{-1}). We detected water (peak S/N = 4.8) and carbon monoxide (S/N = 2.7), with a combined $CO + H_2O$ S/N of 5.9 in our NIRSPEC spectra using the cross-correlation method. The CCF wings for CO and H_2O are largely attributed to the CO band and H_2O, roughly separated by their line widths, which can also be seen in the corresponding autocorrelation functions (ACFs). We were unable to detect CH_4 in our NIRSPEC spectra (S/N = 0.7) due to the relatively large CCF wings of the expected companion velocity as well as a more comparable noise amplitude. The structure in the CCFs for the primary species can be used to further enhance the detection confidence, in the context of forward models, and so we reexamine if CH_4 is present in our NIRSPEC spectra of HD 33632 Ab using the retrieval method described in Section 5. We examined telluric variations that cause false positive detection by excluding telluric strong regions (transmission < 0.4) and found similar S/Ns for all of the species examined above. To further illustrate our confidence in the detection of HD 33632 Ab in our KPIC spectra, we also show CCFs of the best-fit BT-Settl model and baseline forward retrieval CO and H_2O models, and found CCF S/Ns of 6.1 and 7.8, respectively (see Sections 4 and 5 for details of deriving the best-fit models).

4. Forward-modeling Method

To extract the physical parameters of the brown dwarf companion, we used a forward-modeling framework to joint fit the stellar speckle and companion fluxes with the Earth's atmospheric and NIRSPEC instrumental broadening profiles due to the star companion flux contrast $\Delta Ks = 10.2$ mag. This forward-modeling method has been adopted in several high-resolution and medium-resolution spectrometers for close brown dwarf companions and exoplanets, including Keck/KPIC (Wang et al. 2021, 2022; Xuan et al. 2022; Ruffio et al. 2023; Wang et al. 2023; Xuan et al. 2024), the Very Large Telescope (VLT)/CRIRES+ (Landman et al. 2024), Keck/OSIRIS (Ruffio et al. 2019; Wilcomb et al. 2020; Ruffio et al. 2021; Hoch et al. 2023), VLT/SINFONI (Petrus et al. 2021), and VLT/HiRISE (Vigan et al. 2024). This method is particularly useful for modeling low-S/N data as our companion flux is lower than the speckle flux (see below). We analyzed the NIRSPEC spectral orders 31 (2.43–2.49 μm), 32 (2.36–2.41 μm), and 33 (2.29–2.34 μm). Following Wang et al. (2021), our forward model is shown in the equation below:

$$F[p] = \left[\alpha_p \times \left(M\left[p^*\left(\lambda\left[1 + \frac{\mathrm{RV}^*}{c}\right]\right), T_{\rm eff}, \log g\right] \otimes \kappa_R(v \sin i)\right) \times T[p^*(\lambda)]\right] \otimes \kappa_G(\Delta\nu_{\rm inst} \times \sigma_{\rm scale}) + \alpha_{s,f} \times D_s[p^*(\lambda)]. \quad (1)$$

Here, $p^*(\lambda)$ is the pixel as a function of wavelength λ from our wavelength calibration, M is the self-consistent stellar atmosphere model grids as a function of effective temperature $T_{\rm eff}$ (K) and surface gravity $\log g$ (cgs dex), which is then convolved with the projected rotational velocity $v \sin i$ ($\otimes$ denotes convolution, with κ_R as the rotational broadening kernel), corrected for RV*.[16] The companion model is then corrected for the companion scale factor α_p to fit its observed flux contribution, and multiplied by the spectra response $T[p^*(\lambda)]$ (derived from the observed A0V telluric standard star spectra). We then model the stellar flux scale factor $\alpha_{s,f}$ for each fiber f to model the speckle flux contribution $D_s[p^*(\lambda)]$ in the data (i.e., two speckle flux scale factors because there are two fibers observed[17]), the instrumental profile scale term $\sigma_{\rm scale}$ for the instrumental profile $\Delta\nu_{\rm inst}$ (κ_G is the Gaussian broadening kernel), and the noise jitter term in each order. The speckle flux $D_s[p^*(\lambda)]$ is directly drawn from our observed on-axis star flux, which also includes telluric absorption. The term $\sigma_{\rm scale}$ is to account for the nonsymmetric line-spread function in the spatial and spectral directions (Trujillo et al. 2001). We measured the line-spread function in the spatial direction in the trace profile during our data reduction, and found that the spectral direction is typically larger by $\sim$10% (Wang et al. 2021). Additionally, we include the noise jitter term $\sigma_{\rm jitter}$, sampled in log space, and combined it with the extracted noise in quadrature for each order. Therefore, there are 17 parameters in our full forward model, including five parameters for the companion, and 12 parameters for the star and nuisance parameters, since we model three NIRSPEC orders (orders 31–33).

[16] The RV* here is uncorrected for barycentric velocity, which we corrected after the forward-modeling routine and reported in Table 2.

[17] We typically observe the star and companion using two fibers to enable pair subtraction.

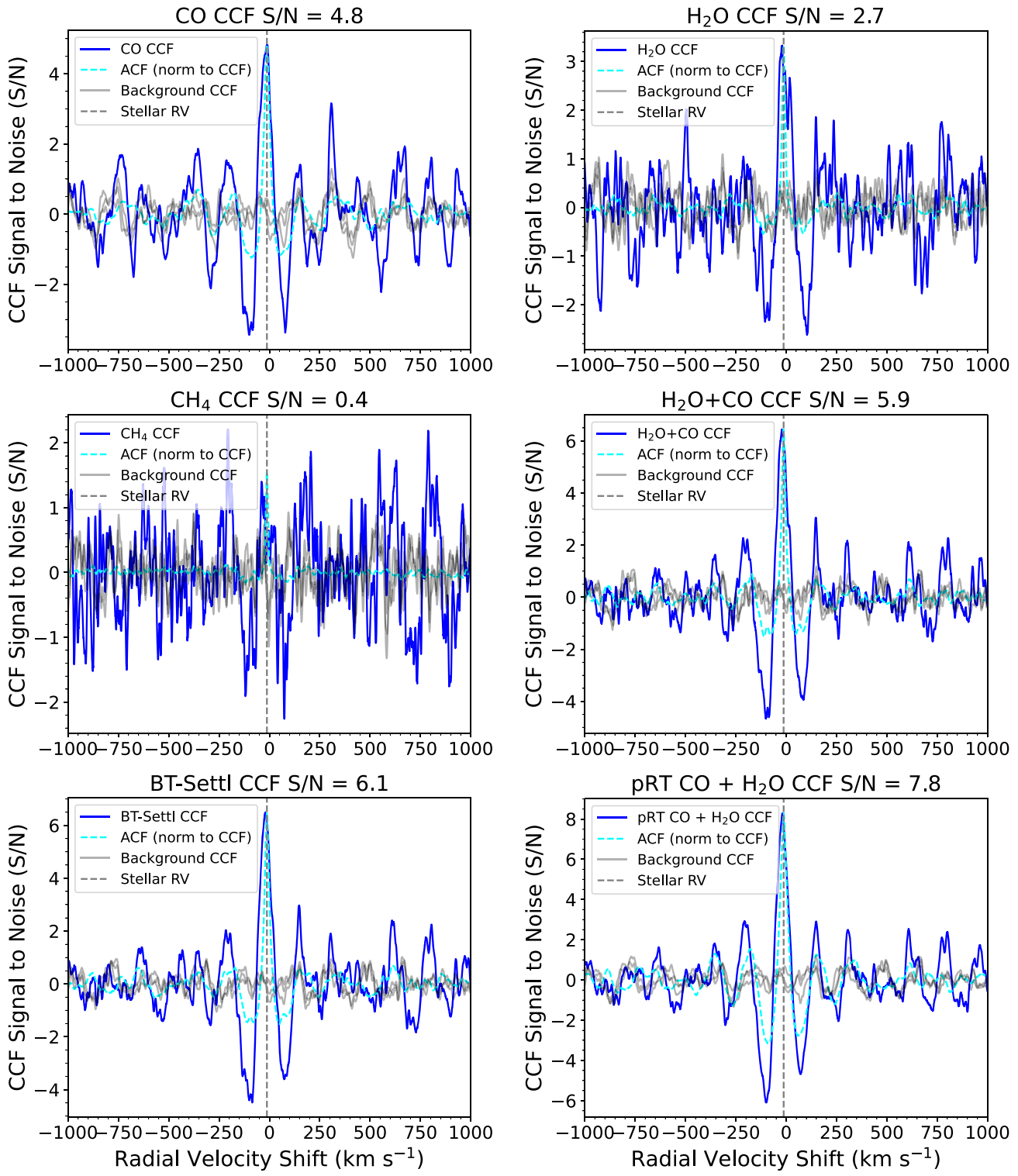

Figure 1. CCF of our KPIC spectrum of HD 33632 Ab with the molecular templates derived from the Sonora–Bobcat models (Marley et al. 2018, 2021). Upper left: CCF (blue solid line) of our KPIC spectra with respect to the CO molecular templates. The background CCFs of three locations are shown in gray lines. The stellar barycentric-included RV (-12.65 km s^{-1}) is depicted by the vertical dashed gray line. The ACF of the CO molecular templates, normalized to the peak of CCF, is plotted as the dashed cyan line. Upper right: same as the upper-left panel for the H_2O molecular templates. Middle left: same as the upper-left panel for the CH_4 molecular templates. Middle right: same as the upper-left panel for the CO and H_2O combined molecular templates. Lower left: same as the upper-left panel for the best-fit BT-Settl models (Section 4). Lower right: same as the upper-left panel for the CO and H_2O combined molecular templates from the best-fit forward-retrieval model (Section 5).

Table 2
HD 33632 Ab NIRSPEC Measurements

UT Date	MJD[a]	Exposure (s)	Throughput[b] (%)	Orders	Model[c] (K)	$T_{\rm eff}$ (cm s^{-2})	log g (km s^{-1})	RV[d] (km s^{-1})	v sin i	Bayes Factor[e]	χ^2
2021 Sep 18	59475.620	5400	1.3	31–33	B	1169^{+130}_{-95}	$4.0^{+0.6}_{-0.3}$	-10 ± 4	63^{+8}_{-7}	1.0	21,289
…	…	…	…	…	S	1800^{+118}_{-104}	$5.2^{+0.2}_{-0.4}$	-12^{+4}_{-5}	55^{+6}_{-7}	0.01	21,317
2021 Nov 20	59538.436	14400	2.4	31–33	B	1473^{+24}_{-38}	$5.33^{+0.12}_{-0.20}$	-8 ± 3	53 ± 3	1.0	19,784
…	…	…	…	…	S	1882^{+75}_{-68}	$5.41^{+0.07}_{-0.14}$	-7 ± 2	53 ± 3	1.3×10^{-6}	19,812

Notes.
[a] MJD at the middle of the observing sequence.
[b] The end-to-end throughput. Our typical KPIC performance is 2%–3%, and <2% is considered poor performance.
[c] The self-consistent substellar atmosphere model grid. "B" is the BT-Settl CIFIST model (Allard et al. 2012) and "S" is the Sonora model (Marley et al. 2021).
[d] Barycentric RV.
[e] We used the BT-Settl CIFIST model (Allard et al. 2012) as our baseline model for each night to compute the Bayes factor.

Our log-likelihood function $\mathcal{L}$ is defined as:

$$\ln \mathcal{L} = -0.5 \times \left[\sum \chi^2 + \sum \ln (2\pi (\sigma^*)^2)\right], \quad (2)$$

where χ^2 is the chi-squared defined as the square of the data minus the full forward model over the inflated noise σ^*. The second term is the normalization constant with the inflated noise.

The brown dwarf atmosphere models are drawn from the BT-Settl (Allard et al. 2012) and Sonora (Marley et al. 2021) models with resolutions of ∼235,000 and ∼200,000, respectively, both assuming solar metallicity. We linearly interpolated the model grid points across different $T_{\rm eff}$ and log g, and used the nested sampling method (Skilling 2004, 2006) with the `dynesty` package (Speagle 2020) to derive our best-fit parameters. We used 1000 live points to sample and followed the default stopping criteria when the difference of log evidence between iterations is below $\epsilon = 1.009$.[18]

We used uniform distributions for our nested sampling priors. Basically, we covered the reasonable parameter range for the $T_{\rm eff}$ from 800 K to 2400 K and log g from 3.5 to 5.5 dex cgs, RV from −100 to +100 km s^{-1}, and v sin i from 0 to 100 km s^{-1}. The companion scale factor α_p ranges from 0 to 100 in data numbers (DN), the speckle scale factors $\alpha_{s,f}$ range from 0 to 6180 DN (for each fiber and each order; six parameters in total), the instrumental profile scale factor goes from 1.0 to 1.2 (for each order; three parameters in total), and the noise jitter is drawn from 0.1 to 30 DN (for each order; three parameters in total).

We modeled the data observed on 2021 September 18 (UT) and 2021 November 20 (UT), with the results shown in Table 2. As noted in Section 2, the data on 2021 September 18 were much worse (lower throughput; S/N = 13) than those from 2021 November 20 (S/N = 20), so the measurements from 2021 September 18 listed in Table 2 are presented largely for completeness, and we adopt our results from 2021 November 20 measurements for the corresponding analysis.

Our forward-modeling best-fit model and posterior probability distributions with the BT-Settl are shown in Figures 2–3.[19] Figure 2 shows that our best-fit forward models match the data well, and our residual (data − model) ACFs are consistent with uncorrelated noise. Our companion flux is lower than the speckle flux by 3.5–5.4×, depending on the order, but the companion model clearly shows the CO (ν2–0) bandhead in order 33 around 2.3 μm, which validates the CO detection in Section 3. The modeled v sin i of 53 ± 3 km s^{-1} indicates that HD 33632 Ab is a relatively fast rotator, which we discuss in detail in Section 7. The best-fit companion RV (-8 ± 3 km s^{-1} shows evidence of orbital motion compared to its primary RV (-1.75 ± 0.12 km s^{-1}; Gaia Collaboration et al. 2023),[20] which we will later constrain the associated orbital parameters in Section 6. Our log $g = 5.33^{+0.12}_{-0.20}$ cgs dex for the BT-Settl model and log $g = 5.41^{+0.07}_{-0.14}$ for the Sonora model hit the surface gravity ceiling of the model grids, which is a typical fitting issue when using self-consistent model grids for field late M, L, and T dwarfs in K-band high-resolution spectra (Del Burgo et al. 2009; Burgasser et al. 2016; Hsu et al. 2021, 2024). The high surface gravity, at a constant mass, represents the small radius issue in the retrievals in Section 5. The modeled $T_{\rm eff}$ values are very different, $T_{\rm eff} = 1473^{+24}_{-38}$ K for the BT-Settl model and $T_{\rm eff} = 1882^{+75}_{-68}$ K for the Sonora model. The BT-Settl models incorporate clouds, while the Sonora models are cloudless, and the difference in $T_{\rm eff}$ among these two models is similar to the findings from T dwarf high-resolution K-band spectra in Hsu et al. (2021). Notably, the BT-Settl $T_{\rm eff}$ estimates have an abrupt drop in the posterior, due to the model treatment of chemistry change at the L–T transition, and its $T_{\rm eff}$ is also consistent with the spectral type estimate of L9.5$^{+1.0}_{-3.0}$ from Currie et al. (2020).

One advantage of the nested sampling method is that we can use the Bayes factor to compare which model is more favored. If the Bayes factor, defined by the ratio of the evidence of two competing models, is smaller by 100 times, the model in the denominator (smaller evidence) is decisively rejected (Jeffreys 1961; Kass & Raftery 1995). We found the BT-Settl models are decisively favored over the Sonora models (Δ Bayes factor $= 1.3 \times 10^{-6}$, and the χ^2 (19,784 versus 19,812) also supported the same conclusion). Therefore, we adopted the best-fit parameters from the BT-Settl models using the 2021 November 20 data, for which RV $= -8 \pm 3$ km s^{-1} and v sin $i = 53 \pm 3$ km s^{-1}.

While we forward modeled the starlight contribution using the observed on-axis star flux, there might be residual starlight that was not completely taken into account in our modeling

[18] $\epsilon = 10^{-3} \times (K - 1) + 0.01 = 1.009$, where $K = 1000$ is the number of nested sampling live points (Speagle 2020).
[19] For completeness, the best-fit spectra with the Sonora model are shown in Figure A2.
[20] While we observed on-axis KPIC spectra for the host star, measuring its RV and v sin i is not possible because the stellar absorption lines are very shallow for F8V HD 33632 in the wavelength used in our analysis.

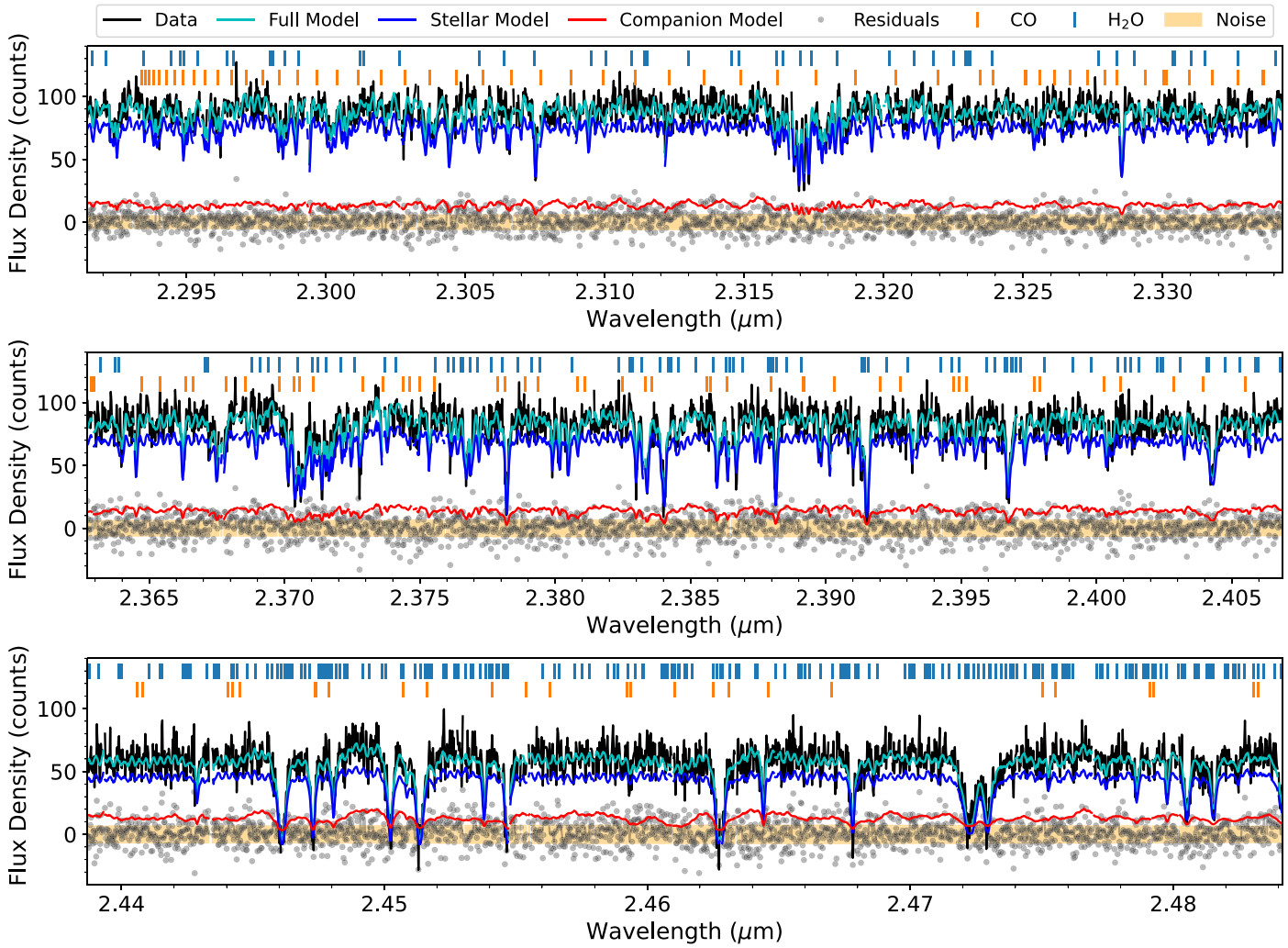

Figure 2. KPIC spectrum of HD 33632 Ab and its best-fit forward model derived from the BT-Settl model grids. The data were taken on 2021 November 20 (UT). The spectral orders 31–33 from fiber 1 are shown in black lines. The full forward model, including the stellar speckle and companion fluxes, is shown as the cyan lines. The stellar model pulled directly from the observed on-axis KPIC spectrum of HD 33632 A, is shown as the blue lines. The planet model, which is the best-fit BT-Settl model with the observed telluric profile, is illustrated in red lines. The residuals (data – full forward model) are plotted as gray dots, consistent with uncorrelated noise, whereas the data noise are shown in the orange shaded region. The CO and H_2O features are labeled in vertical orange and light blue lines, respectively.

framework, such as the temporal variations of the slightly different airmasses between observing the companion and the host star, humidity variations within the full observation, and the difference in optical paths between these frames. Our host star is an F8V star (Gray et al. 2003), with an effective temperature of ∼6180 K (Pecaut & Mamajek 2013). Such a temperature is not expected to present any strong molecular features with only a few weak absorption lines ($\lesssim$10% absorption) in the wavelength range used in our analysis, which we also validated when modeling the observed on-axis star spectra. The observed on-axis star spectra contain mostly telluric absorption features with the fringing modulation.

5. Retrieval Method

While the cross-correlation method provides evidence of CO and H_2O in the atmosphere of HD 33632 Ab, their abundances cannot be constrained (Section 3). Furthermore, it is unclear whether methane is present, or not, in our KPIC data of this L–T transition object. These goals can be achieved with a forward-modeling retrieval method. Here, the package `petitRADTRANS` (Mollière et al. 2019; Nasedkin et al. 2024a) is used to perform our retrieval analysis, following the analysis outlined in Xuan et al. (2022), with slightly different priors listed in Table 3. We measured the CO and H_2O abundances and placed an upper limit on the nondetection of CH_4. Three combinations of data were considered for our retrievals, including (1) retrievals with the high-resolution *K*-band spectra, (2) joint fitting the high-resolution *K*-band spectra and *JHK*-band photometry, and (3) joint fitting the high-resolution *K*-band spectra and low-resolution near-infrared spectra.

5.1. Retrieval Setup for High-resolution Spectra

Our HD 33632 Ab spectra are retrieved with a forward-retrieval modeling framework similar to Section 4. We fit the same NIRSPEC orders 31–33 using the data from 2021 November 20 (UT) by fitting an atmosphere model generated from the retrievals, for which we adopted the pressure–temperature (*P-T*) profile from Mollière et al. (2020). The

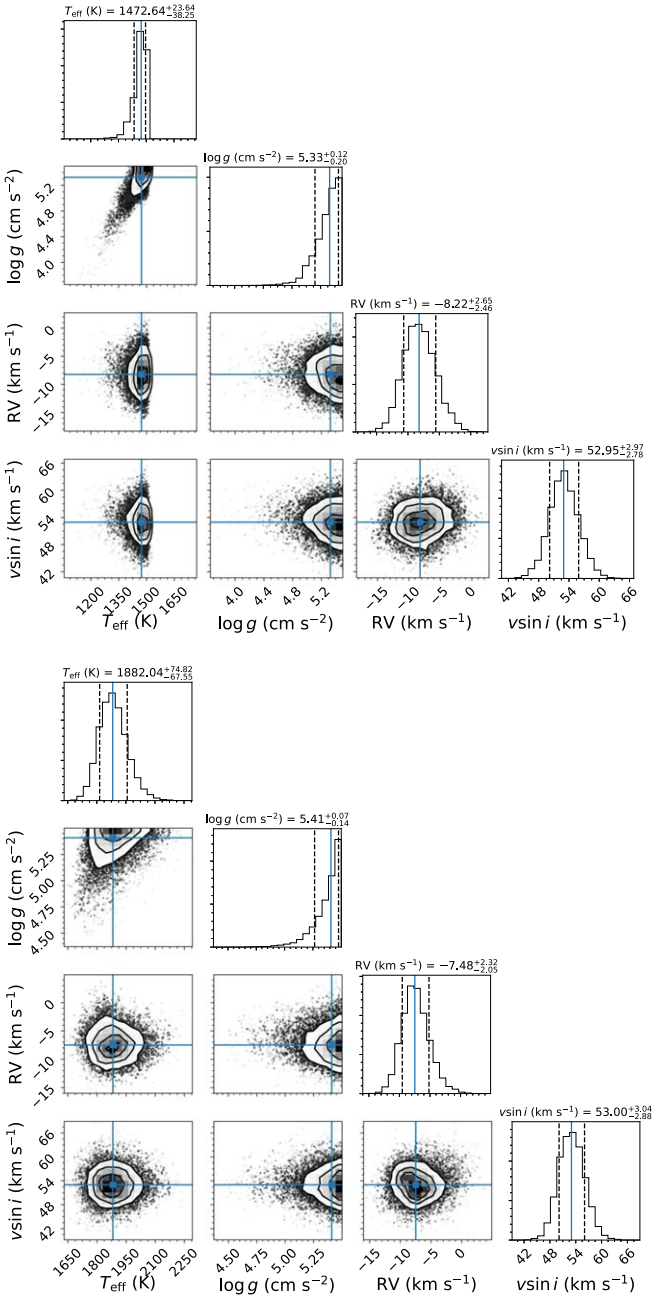

Figure 3. Posterior probability distributions for the substellar parameters of HD 33632 Ab using the BT-Settl (top) and Sonora (bottom) models. The KPIC data were taken on 2021 November 20 (UT). The spectral orders 31–33 from fiber 1 are shown as black lines, while the blue lines indicate the median values and the dashed lines denote the 16th and 84th percentiles.

optical depth τ is given as $\tau = \delta P^{\alpha}$, where P is the pressure and α and δ are free parameters. At middle altitudes, the internal temperature $T_{\rm int}$, using the Eddington approximation, follows $T(\tau)^4 = \frac{3}{4}T_{\rm int}^4(\frac{2}{3} + \tau)$. At high altitudes between $P = 0.1$ bar and $\tau = 0.1$, cubic spline interpolation is used to sample in equidistant location log P space using three parameters, T_1, T_2, and T_3. We log sample our pressure grid from 10^{-5} to 10^{2} bar.

The major opacity species of L–T transition objects in K band are CO, H_2O, and CH_4, so we included line-by-line species for all CO isotopologues ("CO_all_iso"), the principal H_2O isotopologue ("H2O_main_iso") from the HITEMP database (Rothman et al. 2010), and the parent $^{12}CH_4$ species from Hargreaves et al. (2020; "CH4_hargreaves_main_iso"). We also included the Rayleigh scattering species for hydrogen and helium (Dalgarno & Williams 1962; Chan & Dalgarno 1965), as well as continuum collision-induced absorption opacities for H_2–H_2 and H_2–He (Gray 2008). The opacities have a resolution of $R = 10^6$, so we downsampled the opacity table by a factor of 4 to speed up the computations, as this resolution remains sufficiently high with respect to our KPIC spectra, for which $R \sim 35{,}000$. The sampled wavelength range for emission retrieval spectra is 2.28–2.50 μm to cover all three NIRSPEC orders.

Four chemistry scenarios were considered. One is a chemical equilibrium model. The second is a chemical nonequilibrium model, parameterized by the quench pressure

Table 3
Forward Retrieval Modeling Priors

Description	Symbol (Unit)	Priors[a]
Mass	M ($M_{\rm Jup}$)	$\mathcal{N}(46.4, 8)$[b]
Radius[c]	R ($R_{\rm Jup}$)	$\mathcal{U}(0.6, 1.4)$
…	…	$\mathcal{N}(0.86, 0.03)$
Projected rot. vel.	v sin i (km s^{-1})	$\mathcal{U}(0, 100)$
RV	RV (km s^{-1})	$\mathcal{N}(-100, 100)$
Carbon/oxygen[d]	C/O	$\mathcal{U}(0.1, 1.7)$
Metallicity[d]	[C/H]	$\mathcal{U}(-1.5, 1.5)$
Mass fraction of CO	$m_{\rm CO}$	$\mathcal{U}(10^{-7}, 10^{-1})$[e]
Mass fraction of H_2O	m_{H_2O}	$\mathcal{U}(10^{-7}, 10^{-1})$[e]
Mass fraction of CH_4	m_{CH_4}	$\mathcal{U}(10^{-10}, 10^{-1})$[e]
Internal temperature	$T_{\rm int}$ (K)	$\mathcal{U}(500, 3000)$
T_3	T_3 (K)	$\mathcal{U}(0, T_c)$[f]
T_2	T_2 (K)	$\mathcal{U}(0, T_3)$
T_1	T_1 (K)	$\mathcal{U}(0, T_2)$
α	α (mas)	$\mathcal{U}(1, 2)$
log δ[g]	log δ	$P_{\rm phot} \in \mathcal{U}[10^{-3}, 100]$
Quench pressure[h]	$P_{\rm quench}$ (bar)	$\mathcal{U}(10^{-4}, 10^{3})$
Mass frac. of $MgSiO_3$	log $\tilde{X}_{MgSiO_3}$	$\mathcal{U}(-2.3, 1.0)$
Vert. eddy diff. coeff.	log K_{zz} (cm s^{-2})	$\mathcal{U}(5, 13)$
Sediment fraction	$f_{\rm sed}$	$\mathcal{U}(0.0, 10.0)$
Scatter of particle size	σ_g	$\mathcal{N}(37.895, 0.026)$
Companion flux	Companion flux (DN)	$\mathcal{U}(0, 100)$
Speckle flux for fiber 1[i]	Speckle flux (DN)	$\mathcal{U}(0, 6180)$
Speckle flux for fiber 2[i]	Speckle flux (DN)	$\mathcal{U}(0, 6180)$
Scale term for LSF[i]	LSF σ	$\mathcal{U}(1.0, 1.2)$
Error jitter[i]	Error jitter (DN)	$\mathcal{U}(0.1, 30.0)$

Notes.
[a] $\mathcal{N}$ stands for normal priors with the mean and standard deviation in the parentheses, while $\mathcal{U}$ represents uniform priors with the lower and upper bounds in the parentheses. LSF is line spread function.
[b] Mass measurements from Currie et al. (2020).
[c] We have two different radius priors, one with a wider range of uniform priors and the other with a narrow range of normal priors from Baraffe et al. (2003)'s evolutionary models. See Section 5 for details.
[d] Parameters are fitted in chemical equilibrium and in chemical disequilibrium with quench pressure.
[e] Sampled in log space.
[f] T_c is the connection temperature used to connect the photosphere boundary with the Eddington approximation $T_3 = \left(\frac{3}{4}T_{\rm int}^4 \times (0.1 + \frac{2}{3}\right)^{\frac{1}{4}}$.
[g] Log optical depth log δ was sampled from a uniform distribution of the photospheric pressure $P_{\rm phot}$ where the optical depth $\tau = 1$ and $\delta = P_{\rm phot}^{-\alpha}$. See the discussion and justification of these parameters in Mollière et al. (2020).
[h] Only used when the quench pressure is used to model the disequilibrium chemistry.
[i] A separate parameter was used for each order (for orders 31–33).

$P_{\rm quench}$ (Mollière et al. 2020). $P_{\rm quench}$ treats the abundances of CO, H_2O, and CH_4 as constant above a given pressure level, as the timescales of the chemical reactions are longer than the mixing timescale (Zahnle & Marley 2014). The last two retrievals are free chemistry retrievals, which fit each species as a constant across all pressure levels. To examine any potential CH_4 present in our high-resolution spectra, we ran two sets of free retrievals, including (1) CO, H_2O, and CH_4 and (2) CO and H_2O. To compute the [C/H] metallicity under free retrievals, we adopted the solar value of carbon (8.43 ± 0.05) from Asplund et al. (2009).

For our cloud assumptions, we explored cloudless, and the EddySed cloud models from Ackerman & Marley (2001) with two particle shapes for $MgSiO_3$. Our choice of $MgSiO_3$ is motivated by the investigation of the cloudy L dwarf HD 4747 B in Luna & Morley (2021), who found that $MgSiO_3$ is the dominant species in L–T transition objects (Gao et al. 2020; Marley et al. 2021). The first cloud model assumes amorphous spherical particles under Mie scattering (am), while the second cloud model has crystalline irregular shape particles using the distribution of hollow spheres method (cd; Min et al. 2005, 2016). Four parameters are fitted in the EddySed cloud model, including the cloud mass fraction of $MgSiO_3$ ($\tilde{X}_{\rm MgSiO_3}$), the vertical Eddy diffusion coefficient K_{zz}, the sedimentation efficiency factor ($f_{\rm sed}$), and the lognormal size distribution of the particles σ_g.

The mass, radius, and parallax of HD 33632 Ab are required to compute emission spectra. We assume the mass $46 \pm 8\ M_{\rm Jup}$ from Currie et al. (2020) as a Gaussian prior. For our radius, we adopted a uniform prior between $1.0 \pm 0.4\ R_{\rm Jup}$. We used the Gaia Data Release 3 (DR3) parallax 37.895 ± 0.026 mas (Gaia Collaboration et al. 2023), but this has a minimal effect on our retrievals as our NIRSPEC spectra are normalized and not flux calibrated.

Finally, we produce our substellar emission spectral model M from `petitRADTRANS`. The full forward-retrieval model is simply generated by replacing the companion substellar atmosphere term M in Equation (1). We considered a total of 24 models for high-resolution spectral retrievals, including four chemistry models, three cloud assumptions, and two radius priors (Section 5.2). For joint retrievals, we consider 11 scenarios, which are a subset of the high-resolution retrievals (Section 5.3). Table 3 lists the priors of our forward-retrieval modeling method. As there are 25–30 parameters in our forward-retrieval model, nested sampling with `dynesty` is used to obtain our best-fit models and posteriors, which is suitable to sample multimodal and high-number parameter models. We used $K = 200$ live points to run our nested sampling, with the multiellipsoid bounding method to account for multimodel posteriors, and the random walk sampling method. The stopping criteria are the default from `dynesty`, using 1% of the unaccounted evidence remaining and parameterized by the difference of log evidence $\Delta \ln z$ under 0.209 (i.e., $10^{-3} \times (K-1) + 0.01 = 0.209$) for all of our fitting routines (Speagle 2020).

5.2. High-resolution Retrieval Results

In an attempt to minimize bias in our estimates of C/O and [C/H] for HD 33632 Ab, several retrievals were conducted to ensure the robustness of our retrieved parameters, including different chemistry, clouds, radius priors, and data combinations. The full retrieval results are summarized in Table 4.

Our baseline forward-retrieval model assumes cloudless, disequilibrium chemistry parameterized with the quench pressure $P_{\rm quench}$ with a wide uniform radius prior between 0.6 and 1.4 $R_{\rm Jup}$. We found that disequilibrium chemistry is highly favored over the chemical equilibrium model using the Bayes factor (strong $\Delta \ln B = 2.3$–4.6 and decisive $\Delta \ln B > 4.6$; Kass & Raftery 1995). The quench pressure $\log P_{\rm quench} = 2.0 \pm 0.6$ bar indicates a high degree of chemical disequilibrium.[21] The best-fit companion emission spectra are similar to our forward-modeling fits. Our RV ($-8.8^{+2.0}_{-1.9}$ km s^{-1}) and $v \sin i$ (50^{+2}_{-3} km s^{-1}) are consistent within 1σ with our forward-modeling results (RV $= -8 \pm 3$ km s^{-1} and $v \sin i = 53 \pm 3$ km s^{-1}), demonstrating the robustness of our retrieval routine fit. However, our retrieved radius is extremely small, stacked at the lower end of our priors ($\lesssim 0.7\ R_{\rm Jup}$). The small radius issue has been widely reported in the literature (e.g., Gonzales et al. 2018, 2020; Burningham et al. 2021; Hood et al. 2023), which cannot be resolved with sophisticated cloud models (Burningham et al. 2021). As will be shown later in this section, our retrieved abundances, C/O and [C/H], are robust, validated by paralleled sets of retrievals using the restricted Gaussian priors for the radii inferred from the Baraffe et al. (2003) evolutionary models.

Another way to validate our retrieval results is through inspection of our best-fit P-T profiles. Figure 4 shows 100 randomly drawn best-fit P-T profiles from our baseline forward-retrieval models. The inferred effective temperature of our baseline retrieval model is $T_{\rm eff} = 1628^{+109}_{-97}$ K, which is consistent with Sonora models between 1600 and 1800 K near the photosphere and inner atmosphere. However, the P-T profiles in the upper atmosphere of our baseline model are not well constrained compared to those expected from the Sonora models. While in theory the high-resolution spectra should allow us to resolve the line cores of species (but more difficult than the wings due to lower fluxes, thus higher fractional errors) such as the CO bandhead, which can reach into the upper atmosphere (upper panel of Figure 4), the fast rotation of HD 33632 Ab $\sim$50 km s^{-1} smears out the emission contribution of CO lines and thus hinders our ability to constrain the upper atmosphere using our KPIC K-band spectra.

One major goal of using the forward-retrieval modeling method is to possibly detect methane in the L–T transition object HD 33632 Ab. The baseline retrieval result indicates a CH_4 mass fraction of $\log CH_4 = -3.82^{+0.4}_{-1.0}$, almost 30 times lower than the measured CO mass fraction of $\log CO = -2.33 \pm 0.17$, or 15 times lower than the H_2O mass fraction ($\log H2O = -2.62^{+0.19}_{-0.18}$).[22] While the upper and lower bounds of CH_4 are constrained, this does not necessarily mean that we detect methane in our NIRSPEC spectra. Indeed, the low mass fractions for methane in our free retrievals validate the nondetection of methane, with the mass fraction of methane $\log CH_4 = -7.5^{+1.8}_{-1.6}$ to $-8.1^{+1.6}_{-1.2}$. CCFs of a given molecular species against the residual of our data and model without a given species can potentially corroborate if there is indeed no detection of methane, following the technique in Xuan et al. (2022). Therefore, we cross-correlate a given species (CO, H_2O, or CH_4) with the residuals of our KPIC data minus the best-fit retrieval models with/without a given species turned on, as shown in Figure 5.

[21] For completeness, our best-fit spectra and posteriors of our baseline forward-retrieval models are shown in Figures A3 and A4, respectively.

[22] The corresponding volume mixing ratios for CO, H_2O, and CH_4 are -3.34 ± 0.18, $-3.54^{+0.17}_{-0.18}$, and $-5.2^{+0.4}_{-0.6}$, respectively.

Table 4
HD 33632 Ab Forward-retrieval Modeling Results

Chemistry[a]	Cloud[b]	Data[c]	R Prior[d]	Mass ($M_{\rm Jup}$)	Radius ($R_{\rm Jup}$)	$v \sin i$ (km s^{-1})	RV (km s^{-1})	C/O	[C/H]	$m_{\rm CO}$[e]	$m_{\rm H_2O}$[e]	$m_{\rm CH_4}$[e]	$T_{\rm eff}$ (K)	$\log g$ (dex cm s^{-2})	$\log B$[f]
BT-Settl	cloudy	HI	$\mathcal{U}$	…	…	53 ± 3	–8 ± 3	…	…	…	…	…	1473^{+24}_{-38}	$5.33^{+0.12}_{-0.20}$	…
Sonora	cloudless	HI	$\mathcal{U}$	…	…	53 ± 3	–7 ± 2	…	…	…	…	…	1882^{+75}_{-68}	$5.41^{+0.07}_{-0.14}$	…
Chem EQ	cloudless	HI	$\mathcal{U}$	$51.0^{+7.4}_{-7.3}$	$0.67^{+0.12}_{-0.05}$	$48.1^{+2.4}_{-2.2}$	$-7.7^{+1.8}_{-2.1}$	$0.51^{+0.04}_{-0.04}$	$-0.04^{+0.17}_{-0.15}$	$-2.33^{+0.17}_{-0.17}$	$-2.62^{+0.19}_{-0.18}$	$-3.82^{+0.42}_{-0.98}$	1919^{+90}_{-89}	$5.43^{+0.1}_{-0.14}$	−9.4
Chem EQ	cloudless	HI	$\mathcal{G}$	$49.8^{+7.4}_{-6.3}$	$0.85^{+0.03}_{-0.03}$	$53.0^{+2.7}_{-2.7}$	$-7.8^{+2.0}_{-2.3}$	$0.52^{+0.04}_{-0.04}$	$-0.12^{+0.16}_{-0.13}$	$-2.41^{+0.18}_{-0.13}$	$-2.74^{+0.18}_{-0.14}$	$-4.02^{+0.44}_{-0.89}$	1901^{+98}_{-92}	$5.23^{+0.06}_{-0.06}$	
Chem EQ	am	HI	$\mathcal{U}$	$51.9^{+6.2}_{-5.5}$	$0.68^{+0.13}_{-0.06}$	$49.1^{+2.0}_{-2.4}$	$-7.7^{+1.9}_{-2.1}$	$0.53^{+0.04}_{-0.04}$	$0.18^{+0.32}_{-0.26}$	$-2.12^{+0.3}_{-0.3}$	$-2.5^{+0.27}_{-0.2}$	$-3.92^{+0.53}_{-0.63}$	1764^{+157}_{-130}	$5.44^{+0.09}_{-0.19}$	−3.13
Chem EQ	am	HI	$\mathcal{G}$	$49.9^{+7.7}_{-5.7}$	$0.86^{+0.03}_{-0.03}$	$52.8^{+2.6}_{-2.8}$	$-8.1^{+2.2}_{-2.2}$	$0.52^{+0.04}_{-0.04}$	$-0.07^{+0.24}_{-0.16}$	$-2.35^{+0.26}_{-0.17}$	$-2.67^{+0.21}_{-0.17}$	$-4.11^{+0.49}_{-0.67}$	1858^{+113}_{-156}	$5.23^{+0.06}_{-0.06}$	−7.27
Chem EQ	cd	HI	$\mathcal{U}$	$48.8^{+8.2}_{-6.4}$	$0.69^{+0.13}_{-0.07}$	$47.7^{+2.3}_{-2.5}$	$-8.1^{+1.9}_{-2.0}$	$0.51^{+0.04}_{-0.04}$	$-0.04^{+0.19}_{-0.16}$	$-2.34^{+0.21}_{-0.16}$	$-2.64^{+0.19}_{-0.18}$	$-3.87^{+0.4}_{-1.02}$	1891^{+93}_{-85}	$5.4^{+0.11}_{-0.17}$	−5.95
Chem EQ	cd	HI	$\mathcal{G}$	$49.6^{+6.6}_{-6.5}$	$0.85^{+0.02}_{-0.03}$	$51.8^{+2.8}_{-2.9}$	$-6.7^{+1.8}_{-2.0}$	$0.5^{+0.05}_{-0.05}$	$-0.06^{+0.22}_{-0.16}$	$-2.35^{+0.23}_{-0.2}$	$-2.63^{+0.2}_{-0.14}$	$-3.93^{+0.42}_{-0.7}$	1859^{+79}_{-141}	$5.23^{+0.06}_{-0.06}$	−5.76
Pquench	cloudless	HI	$\mathcal{U}$	$47.5^{+6.9}_{-6.9}$	$0.72^{+0.19}_{-0.09}$	$49.6^{+2.2}_{-2.5}$	$-8.8^{+2.0}_{-1.9}$	$0.57^{+0.06}_{-0.05}$	$0.01^{+0.18}_{-0.18}$	$-2.25^{+0.18}_{-0.17}$	$-2.63^{+0.16}_{-0.17}$	$-4.55^{+0.18}_{-0.2}$	1628^{+109}_{-97}	$5.34^{+0.13}_{-0.18}$	0.0
Pquench	cloudless	HI	$\mathcal{G}$	$49.1^{+7.5}_{-6.4}$	$0.86^{+0.03}_{-0.03}$	$55.8^{+2.6}_{-2.4}$	$-8.6^{+1.9}_{-2.0}$	$0.58^{+0.05}_{-0.05}$	$0.0^{+0.19}_{-0.17}$	$-2.26^{+0.19}_{-0.17}$	$-2.64^{+0.17}_{-0.18}$	$-4.59^{+0.19}_{-0.17}$	1614^{+102}_{-94}	$5.22^{+0.06}_{-0.07}$	11.22
Pquench	am	HI	$\mathcal{U}$	$49.1^{+6.7}_{-6.7}$	$0.72^{+0.17}_{-0.09}$	$50.4^{+2.2}_{-2.5}$	$-8.7^{+1.7}_{-1.8}$	$0.57^{+0.05}_{-0.04}$	$0.07^{+0.19}_{-0.16}$	$-2.18^{+0.2}_{-0.16}$	$-2.56^{+0.17}_{-0.15}$	$-4.58^{+0.17}_{-0.18}$	1553^{+107}_{-119}	$5.37^{+0.12}_{-0.19}$	−4.37
Pquench	am	HI	$\mathcal{G}$	$45.2^{+6.5}_{-6.0}$	$0.86^{+0.03}_{-0.03}$	$55.2^{+2.6}_{-2.6}$	$-8.4^{+2.0}_{-2.3}$	$0.59^{+0.04}_{-0.05}$	$0.06^{+0.2}_{-0.18}$	$-2.2^{+0.21}_{-0.18}$	$-2.61^{+0.21}_{-0.21}$	$-4.65^{+0.24}_{-0.29}$	1559^{+95}_{-97}	$5.19^{+0.07}_{-0.07}$	6.56
Pquench	cd	HI	$\mathcal{U}$	$47.8^{+5.7}_{-5.9}$	$0.78^{+0.18}_{-0.13}$	$50.6^{+2.1}_{-2.0}$	$-8.6^{+1.8}_{-1.6}$	$0.57^{+0.05}_{-0.05}$	$-0.04^{+0.21}_{-0.19}$	$-2.3^{+0.19}_{-0.2}$	$-2.68^{+0.2}_{-0.19}$	$-4.71^{+0.24}_{-0.35}$	1621^{+170}_{-158}	$5.29^{+0.17}_{-0.19}$	6.48
Pquench	cd	HI	$\mathcal{G}$	$47.5^{+6.8}_{-6.1}$	$0.87^{+0.02}_{-0.02}$	$54.9^{+2.7}_{-2.7}$	$-7.0^{+1.7}_{-1.8}$	$0.56^{+0.06}_{-0.05}$	$0.03^{+0.19}_{-0.17}$	$-2.24^{+0.2}_{-0.16}$	$-2.58^{+0.14}_{-0.16}$	$-4.65^{+0.22}_{-0.23}$	1535^{+111}_{-133}	$5.19^{+0.07}_{-0.06}$	16.33
C + H + C	cloudless	HI	$\mathcal{U}$	$47.6^{+8.2}_{-7.1}$	$0.76^{+0.19}_{-0.12}$	$50.7^{+2.4}_{-2.6}$	$-9.4^{+2.1}_{-1.9}$	$0.63^{+0.06}_{-0.06}$	$-0.06^{+0.16}_{-0.14}$	$-2.3^{+0.16}_{-0.14}$	$-2.71^{+0.18}_{-0.17}$	$-7.52^{+1.75}_{-1.55}$	2584^{+156}_{-182}	$5.32^{+0.15}_{-0.21}$	8.59
C + H + C	cloudless	HI	$\mathcal{G}$	$50.2^{+6.4}_{-6.1}$	$0.86^{+0.03}_{-0.02}$	$55.4^{+2.6}_{-2.4}$	$-8.8^{+1.8}_{-1.9}$	$0.6^{+0.06}_{-0.06}$	$-0.07^{+0.18}_{-0.18}$	$-2.31^{+0.18}_{-0.18}$	$-2.69^{+0.17}_{-0.16}$	$-7.71^{+1.54}_{-1.39}$	2417^{+269}_{-299}	$5.23^{+0.06}_{-0.06}$	−12.05
C + H + C	am	HI	$\mathcal{U}$	$47.8^{+7.3}_{-6.2}$	$0.76^{+0.22}_{-0.12}$	$50.6^{+2.3}_{-2.4}$	$-8.6^{+2.0}_{-1.9}$	$0.6^{+0.07}_{-0.06}$	$-0.05^{+0.21}_{-0.2}$	$-2.29^{+0.21}_{-0.2}$	$-2.65^{+0.19}_{-0.21}$	$-7.81^{+1.62}_{-1.42}$	2136^{+448}_{-379}	$5.29^{+0.17}_{-0.22}$	9.66
C + H + C	am	HI	$\mathcal{G}$	$47.1^{+6.5}_{-6.4}$	$0.86^{+0.03}_{-0.03}$	$56.8^{+3.0}_{-2.5}$	$-8.7^{+2.5}_{-2.1}$	$0.62^{+0.05}_{-0.05}$	$-0.03^{+0.17}_{-0.17}$	$-2.27^{+0.16}_{-0.17}$	$-2.67^{+0.15}_{-0.16}$	$-7.49^{+1.45}_{-1.48}$	1910^{+616}_{-215}	$5.2^{+0.07}_{-0.07}$	1.4
C + H + C	cd	HI	$\mathcal{U}$	$48.4^{+7.3}_{-6.6}$	$0.72^{+0.2}_{-0.09}$	$50.1^{+2.5}_{-2.5}$	$-8.8^{+1.8}_{-1.8}$	$0.6^{+0.06}_{-0.06}$	$-0.06^{+0.23}_{-0.18}$	$-2.3^{+0.22}_{-0.18}$	$-2.67^{+0.19}_{-0.17}$	$-8.14^{+1.6}_{-1.19}$	1999^{+476}_{-231}	$5.34^{+0.14}_{-0.19}$	4.8
C + H + C	cd	HI	$\mathcal{G}$	$51.4^{+6.1}_{-5.8}$	$0.87^{+0.03}_{-0.03}$	$56.2^{+2.7}_{-2.8}$	$-8.5^{+2.2}_{-1.9}$	$0.6^{+0.06}_{-0.05}$	$-0.1^{+0.15}_{-0.15}$	$-2.34^{+0.15}_{-0.15}$	$-2.72^{+0.15}_{-0.14}$	$-7.8^{+1.59}_{-1.46}$	1883^{+454}_{-214}	$5.23^{+0.06}_{-0.06}$	11.1
C + H	cloudless	HI	$\mathcal{U}$	$43.7^{+5.4}_{-5.4}$	$0.75^{+0.21}_{-0.11}$	$50.5^{+2.0}_{-2.2}$	$-9.4^{+2.2}_{-1.9}$	$0.62^{+0.07}_{-0.06}$	$-0.12^{+0.17}_{-0.17}$	$-2.37^{+0.16}_{-0.17}$	$-2.77^{+0.18}_{-0.17}$	…	2530^{+196}_{-228}	$5.27^{+0.16}_{-0.21}$	9.85
C + H	cloudless	HI	$\mathcal{G}$	$51.9^{+6.2}_{-5.3}$	$0.85^{+0.03}_{-0.03}$	$55.9^{+2.7}_{-2.9}$	$-9.0^{+2.3}_{-2.0}$	$0.62^{+0.06}_{-0.06}$	$-0.06^{+0.17}_{-0.16}$	$-2.3^{+0.16}_{-0.16}$	$-2.69^{+0.16}_{-0.17}$	…	2422^{+230}_{-262}	$5.25^{+0.06}_{-0.06}$	9.17
C + H	am	HI	$\mathcal{U}$	$49.2^{+6.6}_{-6.7}$	$0.71^{+0.17}_{-0.08}$	$51.3^{+2.1}_{-2.1}$	$-9.3^{+1.8}_{-1.6}$	$0.62^{+0.06}_{-0.05}$	$-0.01^{+0.19}_{-0.18}$	$-2.25^{+0.19}_{-0.17}$	$-2.65^{+0.19}_{-0.18}$	…	1832^{+520}_{-172}	$5.36^{+0.13}_{-0.19}$	7.39
C + H	am	HI	$\mathcal{G}$	$53.3^{+4.6}_{-3.7}$	$0.85^{+0.02}_{-0.03}$	$55.8^{+3.1}_{-3.0}$	$-8.4^{+2.3}_{-1.8}$	$0.62^{+0.05}_{-0.06}$	$-0.01^{+0.18}_{-0.19}$	$-2.25^{+0.17}_{-0.19}$	$-2.66^{+0.17}_{-0.16}$	…	1874^{+444}_{-153}	$5.27^{+0.04}_{-0.04}$	10.96
C + H	cd	HI	$\mathcal{U}$	$49.4^{+6.9}_{-6.7}$	$0.75^{+0.21}_{-0.11}$	$50.5^{+2.4}_{-2.6}$	$-8.5^{+2.0}_{-1.8}$	$0.6^{+0.06}_{-0.06}$	$-0.04^{+0.2}_{-0.17}$	$-2.28^{+0.2}_{-0.17}$	$-2.64^{+0.16}_{-0.15}$	…	2169^{+436}_{-399}	$5.32^{+0.14}_{-0.21}$	12.82
C + H	cd	HI	$\mathcal{G}$	$51.1^{+6.2}_{-5.5}$	$0.86^{+0.03}_{-0.03}$	$55.9^{+2.4}_{-2.6}$	$-9.2^{+2.1}_{-1.7}$	$0.63^{+0.05}_{-0.06}$	$0.0^{+0.18}_{-0.16}$	$-2.24^{+0.18}_{-0.16}$	$-2.66^{+0.19}_{-0.17}$	…	1834^{+603}_{-209}	$5.23^{+0.05}_{-0.05}$	1.93
Chem EQ	cd	HI + PH	$\mathcal{G}$	$48.5^{+7.3}_{-6.3}$	$0.83^{+0.03}_{-0.03}$	$53.5^{+2.6}_{-2.7}$	$-8.3^{+1.9}_{-2.1}$	$0.53^{+0.03}_{-0.03}$	$1.08^{+0.23}_{-0.22}$	$-1.25^{+0.22}_{-0.18}$	$-1.71^{+0.16}_{-0.15}$	$-3.43^{+0.23}_{-0.26}$	1316^{+26}_{-27}	$5.24^{+0.07}_{-0.07}$	−22.02
Pquench	cloudless	HI + PH	$\mathcal{U}$	$46.7^{+7.8}_{-6.8}$	$0.65^{+0.07}_{-0.04}$	$55.5^{+2.3}_{-2.5}$	$-8.0^{+1.5}_{-1.6}$	$0.53^{+0.06}_{-0.05}$	$0.86^{+0.24}_{-0.2}$	$-1.43^{+0.21}_{-0.18}$	$-1.82^{+0.19}_{-0.16}$	$-3.92^{+0.23}_{-0.24}$	1391^{+51}_{-68}	$5.41^{+0.1}_{-0.11}$	0.0
Pquench	am	HI + PH	$\mathcal{U}$	$45.9^{+6.8}_{-6.4}$	$0.67^{+0.1}_{-0.05}$	$55.9^{+2.5}_{-2.6}$	$-7.9^{+1.4}_{-2.1}$	$0.54^{+0.05}_{-0.05}$	$0.86^{+0.24}_{-0.29}$	$-1.44^{+0.22}_{-0.26}$	$-1.81^{+0.19}_{-0.22}$	$-3.95^{+0.23}_{-0.22}$	1361^{+76}_{-111}	$5.41^{+0.09}_{-0.14}$	−3.81
Pquench	cd	HI + PH	$\mathcal{U}$	$48.7^{+6.6}_{-5.3}$	$0.69^{+0.11}_{-0.07}$	$54.8^{+2.1}_{-2.2}$	$-8.1^{+1.4}_{-1.8}$	$0.57^{+0.05}_{-0.05}$	$1.06^{+0.22}_{-0.18}$	$-1.27^{+0.19}_{-0.17}$	$-1.66^{+0.13}_{-0.15}$	$-4.03^{+0.28}_{-0.23}$	1296^{+103}_{-160}	$5.4^{+0.08}_{-0.14}$	−3.44
Pquench	cd	HI + PH	$\mathcal{G}$	$47.0^{+6.8}_{-6.9}$	$0.85^{+0.03}_{-0.03}$	$56.1^{+2.6}_{-2.5}$	$-7.9^{+1.3}_{-1.7}$	$0.57^{+0.05}_{-0.05}$	$1.07^{+0.18}_{-0.17}$	$-1.24^{+0.15}_{-0.14}$	$-1.67^{+0.14}_{-0.11}$	$-3.94^{+0.21}_{-0.23}$	1217^{+36}_{-62}	$5.21^{+0.07}_{-0.07}$	−22.4
Chem EQ	cd	HI + LO	$\mathcal{G}$	$47.4^{+6.7}_{-6.4}$	$0.75^{+0.02}_{-0.02}$	$51.3^{+3.1}_{-2.9}$	$-6.9^{+1.6}_{-1.8}$	$0.55^{+0.03}_{-0.04}$	$0.57^{+0.15}_{-0.14}$	$-1.73^{+0.15}_{-0.13}$	$-2.19^{+0.06}_{-0.06}$	$-3.21^{+0.21}_{-0.27}$	1373^{+17}_{-18}	$5.32^{+0.06}_{-0.07}$	−16.25
Pquench	cloudless	HI + LO	$\mathcal{U}$	$43.7^{+6.4}_{-6.9}$	$0.61^{+0.02}_{-0.01}$	$54.8^{+2.5}_{-2.9}$	$-7.6^{+1.9}_{-2.0}$	$0.53^{+0.03}_{-0.03}$	$0.31^{+0.14}_{-0.12}$	$-1.97^{+0.13}_{-0.13}$	$-2.39^{+0.07}_{-0.07}$	$-3.57^{+0.13}_{-0.11}$	1484^{+13}_{-18}	$5.45^{+0.06}_{-0.08}$	0.0
Pquench	am	HI + LO	$\mathcal{U}$	$46.1^{+6.6}_{-7.2}$	$0.61^{+0.02}_{-0.01}$	$54.0^{+3.1}_{-3.5}$	$-5.6^{+1.6}_{-1.8}$	$0.53^{+0.04}_{-0.04}$	$0.35^{+0.15}_{-0.14}$	$-1.94^{+0.16}_{-0.14}$	$-2.36^{+0.07}_{-0.07}$	$-3.55^{+0.12}_{-0.12}$	1478^{+14}_{-21}	$5.48^{+0.06}_{-0.07}$	8.98
Pquench	cd	HI + LO	$\mathcal{U}$	$46.4^{+6.4}_{-6.6}$	$0.61^{+0.02}_{-0.01}$	$53.5^{+2.6}_{-3.1}$	$-6.2^{+1.9}_{-2.1}$	$0.53^{+0.04}_{-0.04}$	$0.32^{+0.14}_{-0.14}$	$-1.96^{+0.14}_{-0.14}$	$-2.38^{+0.07}_{-0.06}$	$-3.55^{+0.1}_{-0.11}$	1475^{+13}_{-16}	$5.48^{+0.06}_{-0.07}$	2.74
Pquench	cd	HI + LO	$\mathcal{G}$	$42.9^{+5.7}_{-6.3}$	$0.76^{+0.02}_{-0.02}$	$53.1^{+2.7}_{-2.5}$	$-7.7^{+1.9}_{-1.7}$	$0.55^{+0.04}_{-0.04}$	$0.54^{+0.16}_{-0.14}$	$-1.76^{+0.17}_{-0.15}$	$-2.21^{+0.06}_{-0.07}$	$-3.3^{+0.09}_{-0.1}$	1360^{+21}_{-21}	$5.27^{+0.05}_{-0.07}$	−24.17

Notes.
[a] Our chemistry settings are (1) "Chem EQ:" chemical equilibrium; (2) "Pquench:" chemical nonequilibrium using the quench pressure from Mollière et al. (2020); (3) "C + H + C:" chemical nonequilibrium using free retrievals of the CO + H_2O + CH_4 molecules; and (4) "C + H:" chemical nonequilibrium using free retrievals of the CO + H_2O molecules.
[b] Our cloud settings are (1) "cloudless:" no clouds; (2) "am:" cloud model from Ackerman & Marley (2001) with the amorphous $MgSiO_3$; and (3) "cd:" cloud model from Ackerman & Marley (2001) with the $MgSiO_3$ condensate.
[c] Our data types are (1) "HI:" high-resolution spectra; (2) "HI + PH:" high-resolution spectra and photometric measurements from Currie et al. (2020); and (3) "HI + LO:" high-resolution spectra and low-resolution spectra from Currie et al. (2020).
[d] Our radius priors include (1) $\mathcal{U}$: the wide uniform priors and (2) $\mathcal{G}$: the restricted Gaussian priors using the Baraffe et al. (2003) brown dwarf evolutionary models.
[e] Mass fractions for CO ($m_{\rm CO}$), H_2O ($m_{\rm H_2O}$), and CH_4 ($m_{\rm CH_4}$).
[f] The Bayes factor of log base 10. Because the Bayes factor depends on the data used in the fit, we set our baseline models using the cloudless disequilibrium "Pquench" retrievals under the wide uniform radius priors for each data combination (HI; HI + PH; and HI + LO).

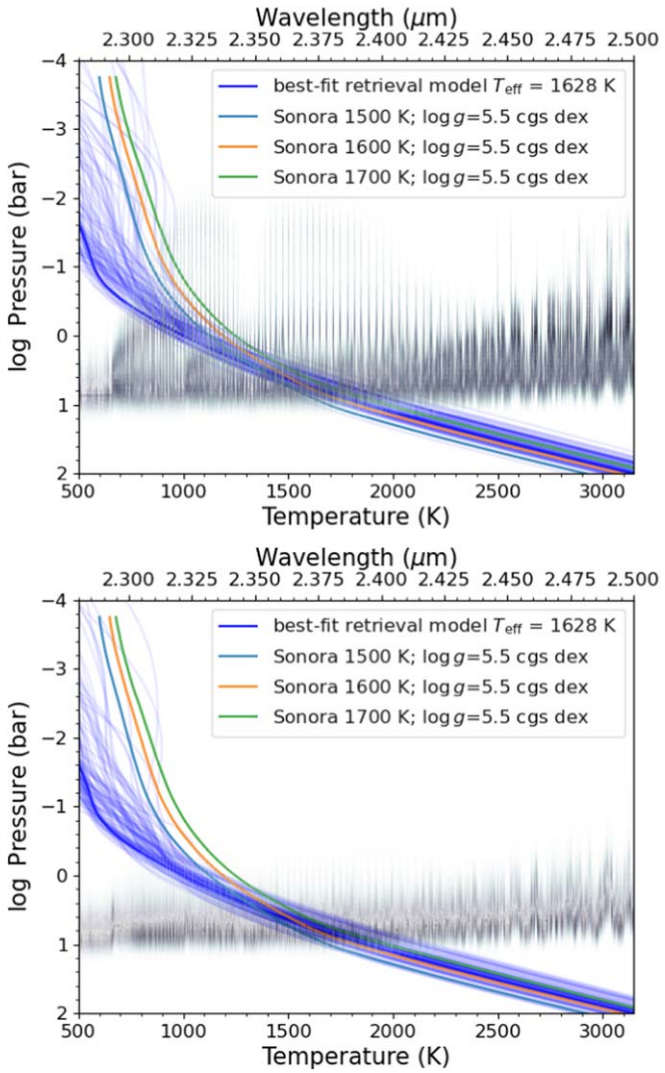

Figure 4. P-T profiles and emission contributions of our baseline forward-retrieval model for HD 33632 Ab. Our P-T profiles are randomly drawn from 100 best-fit baseline forward-retrieval models (blue), and the Sonora models of 1500, 1600, and 1700 K under $\log g = 5.5$ dex cgs in light blue, orange, and green lines, respectively. The emission contribution function (pressure vs. wavelength) without/with rotation included are plotted in the left and right panels, respectively. The fast rotation of HD 33632 Ab limits our ability to constrain the P-T profiles in the upper atmosphere.

Similar to our findings in Section 3, we found clear detections of CO (S/N = 4.6), H_2O (S/N = 2.6), and CO + H_2O (S/N = 7.6), but there is no detection in the CCF for CH_4 (S/N = −1.0).

To validate that our retrieved parameters are robust regardless of our radius priors, we ran the retrievals under the restricted Gaussian radius priors $R_{\rm prior} = 0.86 \pm 0.03$ $R_{\rm Jup}$, with the radii inferred from the Baraffe et al. (2003) evolutionary models. We found that the inferred $v \sin i$ values under the restricted priors are consistent but generally higher by ∼5 km s^{-1} compared to the wide uniform priors. The higher radii from the restricted priors, under the same mass priors, imply a smaller $\log g$. Therefore, higher $v \sin i$ values compensate for the smaller pressure broadening in the line profile. The RVs and retrieved C/O and [C/H] are generally consistent under the wide and restricted radius priors. The posteriors of $\log g$ using the BT-Settl and Sonora models are stacked at the highest available $\log g = 5.5$ dex cm s^2, which has been a common issue in fitting high-resolution spectra at ∼2.3 μm for low-mass field stars and brown dwarfs (e.g., Hsu et al. 2021, 2023, 2024), also implying small radii within the self-consistent modeling grids. It is noted that our forward-model framework that incorporates the on-axis star spectra might still have residual starlight, as discussed in Section 4.

5.3. Retrievals with High-resolution and Joint Fitting Low-resolution Spectra or Broadband Photometry

While we showed that our retrievals using high-resolution spectra are insensitive to the radius priors, we explored whether joint fitting low-resolution spectra or broadband photometry could resolve the small radius issue. Our retrieval setting is similar to Section 5.2, following the prescription in Xuan et al. (2022). The low-resolution spectra and broadband photometry are compiled from the SCExAO/CHARIS data in Currie et al. 2020 (i.e., $J = 16.91 \pm 0.11$, $H = 16.00 \pm 0.09$, $Ks = 15.37 \pm 0.09$ and their Table 2). While our joint-fitting forward-retrieval modeling is similar to that for the high-resolution spectra alone, we included the major molecular absorbers of CO, H_2O, and CH_4 from HITEMP database (Hargreaves et al. 2020), and NH_3, CO_2, FeH, VO (B. Plez), TiO (B. Plez), K (F. Allard), and Na (F. Allard) from (Mollière et al. 2019). The sampled wavelength is between 0.8 and 2.5 μm using the correlated-k sampling method. For broadband photometry, the MKO *JHKs* profiles are multiplied by our broadband, low-resolution retrieval model before computing the log-likelihood.[23] The log-likelihood is the sum of the high-resolution spectra and low-resolution spectra or the broadband photometry. As running these retrievals roughly doubles the computation time, we only examined our baseline combinations of retrievals, which are chemical nonequilibrium with the quench pressure.

Figure 6 and Table 4 compare our forward-retrieval models under a select set of data combinations. Figure 7 shows our baseline joint-fitting retrieval results for the photometry and low-resolution spectra. The continuum from low-resolution spectra or photometry is difficult to reproduce, partly due to residual stellar light contribution (e.g., the AF Lep b low-resolution spectra reported in De Rosa et al. 2023; Mesa et al. 2023). Joint fitting low-resolution spectra or broadband near-infrared photometry with our wide, uniform priors did not resolve the radius issue. The retrieved mass, $v \sin i$, RV, and C/O are consistent. However, the measured metallicities are dependent on the data combination. Retrievals of joint fitting the broadband photometry give [C/H] = 0.85–1.1, while retrievals of joint fitting low-resolution spectra return [C/H] = 0.3–0.6, much higher than our measured metallicity of [C/H] ∼ 0.0 from the high-resolution retrievals. The main reason is that the low-resolution spectra and photometry are more sensitive to either clouds or the deep atmosphere if it is clear. The effective optical depth ties directly to the inferred metallicity, which reflects the [C/H] trend. This effect mirrors the trend for [O/H], via water, which cancels out the C/O estimate. This means that our retrieved C/O is more robust than [C/H], which holds even for a relatively fast rotator such as HD 33632 Ab. As our high-resolution spectra with CO and H_2O molecules anchor our metallicities, we regard the inferred [C/H] values from joint fitting the low-resolution spectra or broadband photometry as not robust. Better characterization or suppression of host starlight for low-resolution spectra in the future might provide us with more consistent results, to precisely model the continuum and thus

[23] http://irtfweb.ifa.hawaii.edu/~nsfcam/filters.html

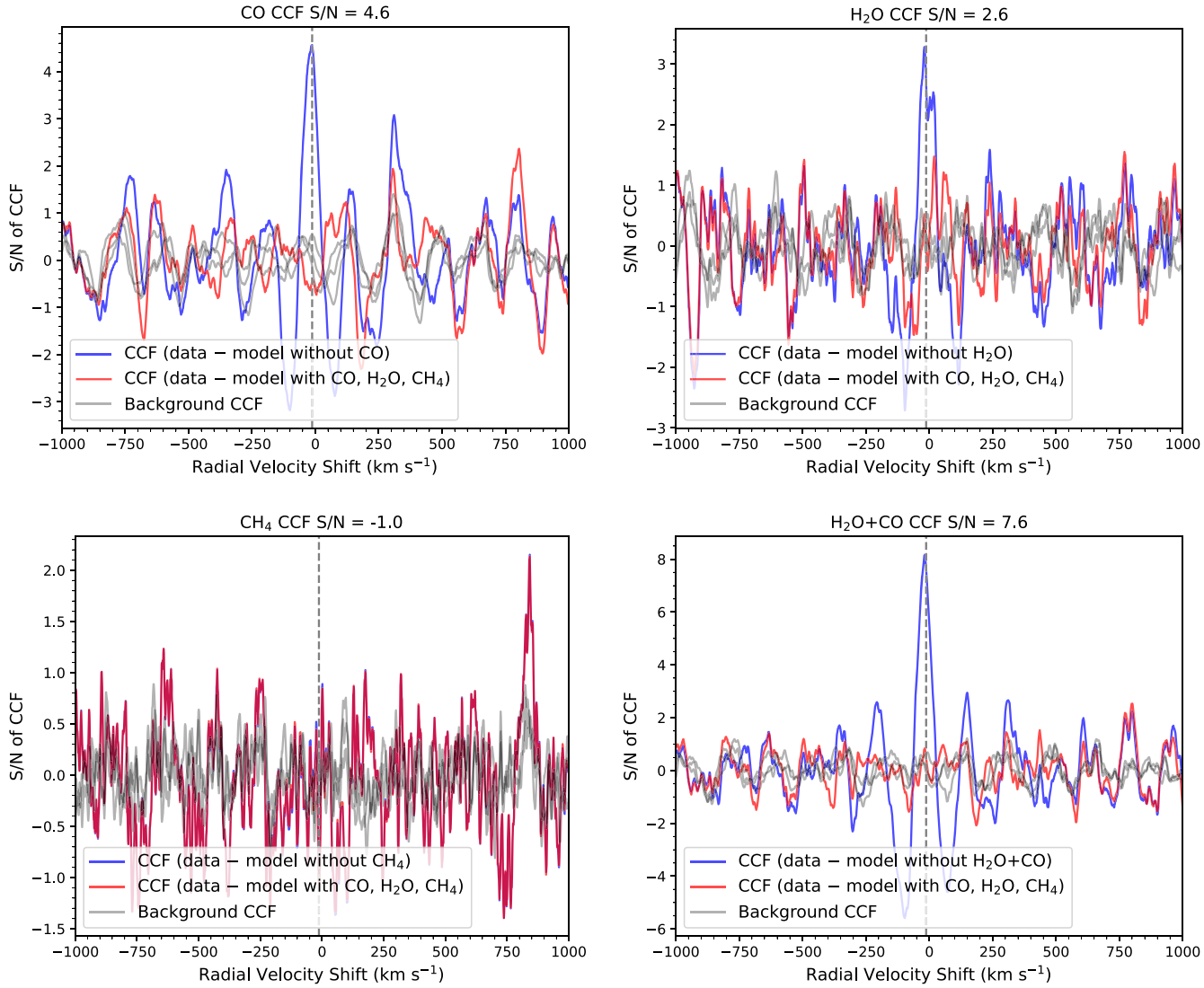

Figure 5. CCFs of the residuals of our KPIC spectrum for HD 33632 Ab using the molecular templates derived from our baseline forward-retrieval model. Upper left: CCFs of the residuals against the CO template. The residuals are defined as the difference between our KPIC data and the best-fit model with all (CO, H_2O, and CH_4) species and without the CO molecules (i.e., H_2O and CH_4 only), which are labeled in red and blue lines, respectively. The background CCFs in three locations on the detector are shown in gray lines. The stellar barycentric-included RV (-12.65 km s^{-1}) is depicted by the vertical dashed gray line. Upper right: same as the upper-left panel, but for H_2O. Lower left: same as the upper-left panel, but for CH_4. Lower right: same as the upper-left panel, for the combined CO + H_2O molecular templates.

clouds of low-temperature objects (e.g., clouds might affect the inferred metallicity; Calamari et al. 2024).

5.4. Effective Temperatures

Comparisons of the effective temperatures inferred in our retrievals allow us to compare these results against self-consistent modeling grids. Our effective temperatures are computed by integrating between the wavelength range of 0.5–30.0 μm. We used the correlated-k method to sample the molecular species used in our low-resolution spectral retrievals (Section 5.3), with the uncertainties computed from the Monte Carlo method.

For $T_{\rm eff}$ inferred from our high-resolution spectral retrievals, the cloudless free retrievals have unphysically high temperatures (∼2400–2500 K). Clouds could mitigate the issue. The $T_{\rm eff}$ values under chemical equilibrium (∼1720–1920 K) are similar to $T_{\rm eff}$ values found using the Sonora models (∼1880 K). Among our high-resolution retrievals, the lowest $T_{\rm eff}$ values are the retrievals parameterized by the quench pressure (∼1550–1630 K), consistent with the $T_{\rm eff}$ values from the BT-Settl model fit (∼1470 K). While our best-fit effective temperatures are generally higher than the L9.5 spectral type (∼1300 K; Mamajek et al. 2013), this could indicate that HD 33632 Ab could be an earlier spectral type than the reported L9.5$^{+1.0}_{-3.0}$ from Curiel et al. (2020), where methane is not yet significantly converted from carbon monoxide. The literature spectral type is uncertain due to relatively low-S/N spectra (∼20–40) with SCExAO/CHARIS from Currie et al. (2020), and the literature spectral type to effective temperature relation has a scatter ∼113 K (Filippazzo et al. 2015). However, we disregard our $T_{\rm eff}$ measured through the high-resolution spectra because our high-resolution spectra are normalized in the fitting routine and not flux calibrated, limited to a narrow wavelength range where the cloud effect is more evident from broadband photometry and wide wavelength coverage. Additionally, the $T_{\rm eff}$ values inferred from high-resolution near-infrared spectra using theoretical stellar/substellar atmosphere models could deviate by

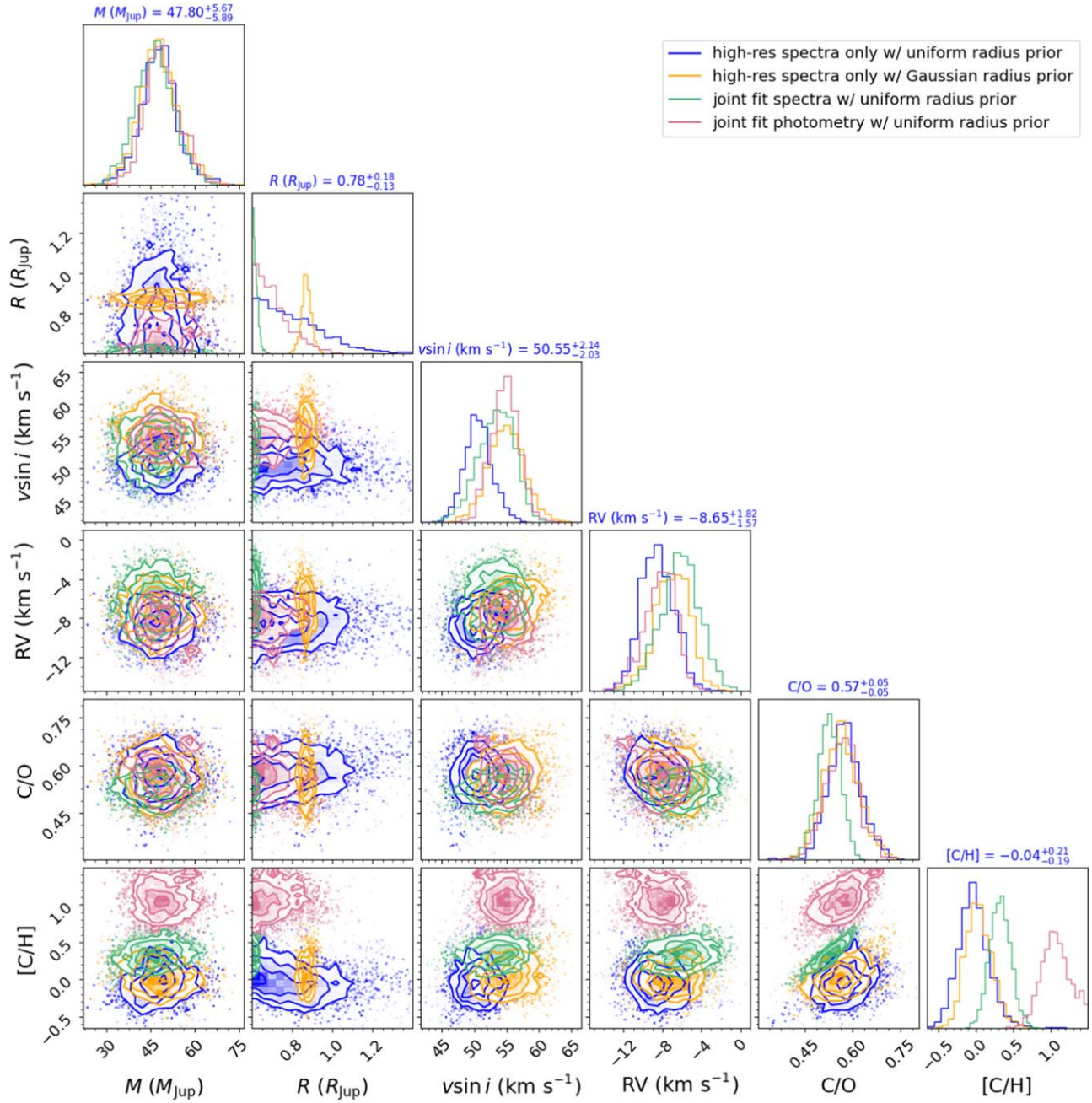

Figure 6. Posterior probability distributions of our retrieval models of HD 33632 Ab for the selected substellar parameters. We compared the retrievals using a combination of high-resolution and low-resolution spectra, as well as photometry. The median values are labeled in solid lines, and the 16th and 84th percentiles are labeled as dashed lines. We compare the following scenarios: high-resolution spectra only for uniform/wide radius priors (blue) and for Gaussian/restricted radius priors (orange); joint fitting high-resolution spectra and low-resolution spectra for uniform/wide radius priors (bluish green); and joint fitting high-resolution spectra and *JHK* photometry for uniform/wide radius priors (reddish purple).

500 K from the expected effective temperatures measured with photometry or low-resolution spectra (Del Burgo et al. 2009; Hsu et al. 2021, 2024). Our joint-fit retrievals with low-resolution spectra and photometry generally imply $T_{\rm eff} = 1200$–1500 K, consistent with the literature spectral type.

5.5. Comparison to Host Star Metallicity and Abundances

Our final goal of the retrieval modeling is to validate whether our inferred metallicity and abundances (C/O ratio) are consistent with the host star. HD 33632 A has several metallicity measurements in the literature. The wide range of metallicity determinations (−0.01 to −0.33 dex) in the literature highlights systematics in the photometric and spectroscopic methods and the corresponding data (Marsakov & Shevelev 1995; Chen et al. 2000; Suchkov et al. 2003; Mishenina et al. 2004; Taylor 2005; Valenti & Fischer 2005; Ammons et al. 2006; Holmberg et al. 2009; Soubiran et al. 2010; Anderson & Francis 2012; Soubiran et al. 2016). Spectroscopic metallicity is generally preferred, as it suffers less from the imprecise parallax measurements compared to other methods (especially in the pre-Gaia era), and these measurements are in good agreement (−0.18 to −0.25) with the reported uncertainties. Among the spectroscopic constraints, we adopted the host star abundance measurements from Rice & Brewer (2020), who reported the only available C and O

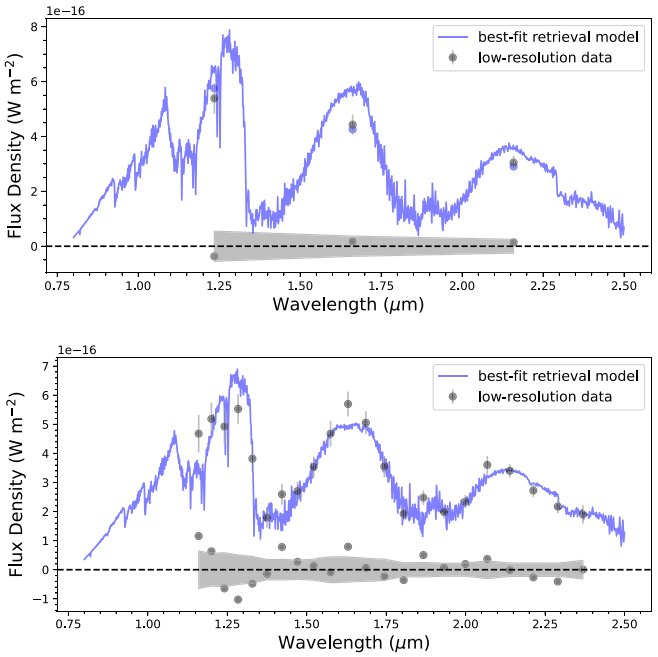

Figure 7. Joint-fitting retrieval results for our baseline models. Top: joint fitting *JHK* photometry. Bottom: joint fitting near-infrared low-resolution spectra. The low-resolution data and photometry were compiled from Currie et al. (2020, black dots). The best-fit model is shown in blue, with the residual (data − model) in black dots near zero and data noise in the gray shaded region.

abundances for HD 33632 A. The abundances obtained with Keck/HIRES spectra using a data-driven method by Rice & Brewer (2020), who trained their sample based on SPOCS measurements (Valenti & Fischer 2005), indicated that [Fe/H] = −0.15 ± 0.03, [C/H] = −0.13 ± 0.05, and [O/H] = 0.01 ±0.07. The inferred C/O ratio = $0.39^{+0.12}_{-0.09}$ with uncertainties propagated by the Monte Carlo method.

In our retrievals with high-resolution spectra, the cloud assumptions typically lower our inferred $T_{\rm eff}$, which can be significant by a few hundred kelvin, but we found consistent C/O and [C/H] regardless of clouds. While the cloudy models are generally favored over the cloudless models, with our high-resolution spectra, cloud signatures are difficult to recover in our high-resolution spectra, as we are fitting only a narrow range of wavelengths near ∼2.3 μm. The low-resolution or photometry joint-fit retrievals do provide more consistent $T_{\rm eff}$ values compared to the expected spectral type, but the measured metallicities and abundances are much higher compared to the retrievals using only high-resolution spectra (Section 5.3). The high-resolution spectra can resolve the molecular lines which enable more accurate abundances, so our adopted C/O and [C/H] are only based on our high-resolution spectral retrievals.

The brown dwarf companion is expected to have the same metallicity and abundances as its host star. In our baseline retrieval, the measured [C/H] = −0.01 ± 0.18 and C/O = 0.57 ± 0.06 for HD 33632 Ab are consistent within 1σ and 1.5σ (or 0.16 dex and 0.18 differences), respectively. Other settings using the high-resolution spectra are consistent with the uncertainties. To realistically quantify the systematics of C/O and [C/H] in our retrieval models, we compared four brown dwarf companions with available host star metallicities observed with KPIC (Wang et al. 2022; Xuan et al. 2022, 2024). We found the average differences of C/O and [C/H] (or [Fe/H]) compared to the host stars of these systems are 0.14 and 0.17, respectively, so we determined the C/O and [C/H] and associated uncertainties for HD 33632 Ab as 0.58 ± 0.14 and 0.0 ± 0.2 dex, respectively.

6. Orbital Analysis

In this section, we present updated orbital solutions for the HD 33632 Ab system. The companion RV, the new astrometry from Gaia DR3, and the EDR3 edition of the Hipparcos–Gaia Catalog of Accelerations (HGCA) from Brandt (2021)[24] are available to refine the orbital solutions since the discovery by Currie et al. (2020). We incorporated the stellar RV from Gaia Collaboration et al. (2023, -1.75 ± 0.12 km s^{-1})[25] and companion RV from our KPIC spectra (-8 ± 3 km s^{-1}), relative astrometry from Currie et al. (2020, three epochs), absolute astrometry, and the Lick RV measurements from Fischer et al. (2014). For the absolute astrometry, we fit Gaia DR3 (Gaia Collaboration et al. 2023) and Hipparcos Intermediate Astrometric Data (IAD; Perryman et al. 1997; van Leeuwen 2007), and the Gaia EDR3 Edition of HGCA from Brandt (2021). The Gaia RV of the host star HD 33632 A is used to compute the relative RV using `orbitize!`. We also fit the overall systematic RV using the Lick RV measurements because their RVs are measured relative to a given epoch (JD 2451206.78125).

For completeness, we also fit the orbital solution without the absolute astrometry and one with the EDR3 HGCA from Brandt (2021), instead of the Gaia and Hipparcos IAD data directly, to examine any possible systematic uncertainties in our approach.

We used the `orbitize!` package (Blunt et al. 2020) to fit for the orbital solutions for the HD 33632 Ab system. Our best-fit orbital parameters are obtained using the Markov Chain Monte Carlo (MCMC) method using the `emcee` (Foreman-Mackey et al. 2013) package. There are 11 parameters in the orbital modeling, including the semimajor axis (SMA; a), eccentricity (e), inclination (i), argument of periastron (ω), position angle (PA) of nodes (Ω), epoch of periastron passage (τ, as a fraction of orbital period), parallax (π), RV offset (γ_0) for the host star RV (to model the systematic RV for the host star), RV error jitters[26] (σ_0 and σ_1) for the host and companion RVs, and the host star mass (m_0).

To fit the orbital solutions, we assumed Gaussian priors for the host star mass ($1.11 \pm 0.09\ M_\odot$;Currie et al. 2020) and the parallax ($\pi = 37.8953 \pm 0.0263$ mas from Gaia DR3; Gaia Collaboration et al. 2023). We assumed uniform priors for the companion mass between 0.0 and 0.1 $M_\odot$. The priors for the remaining parameters used the default setting in `orbitize!`: a with log-uniform priors from 0.001 to 10,000 au; e with uniform priors from 0 to 1; i with a sine distribution (i.e., uniform inclinations); ω with uniform priors from 0 to 2π rad;

[24] We used the recently updated `orbitize!` available on https://github.com/sblunt/orbitize, with the commit 0fb5435. The current `orbitize!` is capable of fitting relative astrometry, companion (relative) RV, Hipparcos IAD data, as well as the HGCA catalog.

[25] The stellar RV is consistent in the literature since 2006–2022, including -1.7 ± 0.2 km s^{-1} (Gontcharov 2006), -1.8 ± 0.3 km s^{-1} (Kharchenko et al. 2007; Casagrande et al. 2011), -1.7 ± 0.1 km s^{-1} (de Bruijne & Eilers 2012), -1.88 ± 0.15 km s^{-1} (Brandt 2021), and -1.9 ± 0.3 km s^{-1} (Tsantaki et al. 2022). While we also observed stellar spectra with KPIC, the stellar features in K band are not useful to derive the RV.

[26] Note that the RV jitter term is to inflate the RV measurements for unaccounted noise, which is a common practice for RV-related orbital fitting (Howard et al. 2014).

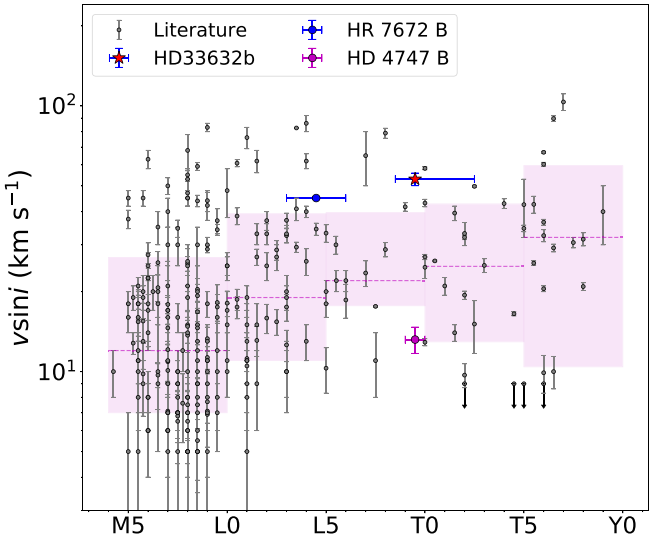

Figure 8. Projected rotational velocities vs. spectral types of VLM objects (M5–T9). The $v \sin i$ measurements are labeled in gray dots, while for the companions published with KPIC, the magenta dot is used for HR 7672 B (Wang et al. 2022), the blue dot for HD 4747 B (Xuan et al. 2022), and the red star for HD 33632 Ab (this work), respectively. The median values of the sample binned per the five subtypes are labeled as dotted magenta lines, with their standard deviations and magenta shaded regions. The majority of this sample is compiled from Crossfield (2014) and Hsu et al. (2021, 2024). See Section 7 for details.

Ω with uniform priors from 0 to π rad; τ with uniform priors from 0 to 1; γ for the host star with uniform priors from -5 to $+5$ km s^{-1}; and RV jitter for host star and companion with log-uniform priors from 0.0001 to 0.05 km s^{-1}. Our MCMC sampler was set with 1000 walkers, 50,000,000 steps (for all walkers), and the first 90% steps were discarded as burn-ins.

Under these assumptions, we adopted the best-fit orbital parameters using the HGCA (EDR3) with both the host and companion RVs, with our updated orbital parameters as $a = 18.4^{+5.2}_{-2.8}$ au, $e = 0.25^{+0.17}_{-0.18}$, $i = 32.94^{+10.98}_{-20.56}$ degrees, $\pi = 37.9 \pm 0.03$ mas, companion mass $m_1 = 36.63^{6.69}_{4.17}$ $M_\odot$, and primary mass $m_0 = 1.11^{+0.09}_{-0.08}$ $M_\odot$. Our adopted best-fit orbit is shown in Figure B1. Figure B2 and Table B1 compare the best-fit orbital solutions for the SMA, eccentricity, parallax, inclination, and primary and secondary masses under various assumptions. For the SMA, we found that the Hipparcos IAD returned very different measurements compared to the other methods, which were attributed to the underestimated uncertainties from the Hipparcos IAD. Therefore, we did not adopt any orbital solutions from the Hipparcos IAD. The HGCA methods provided consistent SMAs compared to the measurements from Currie et al. (2020). Among the HGCA fits, the posteriors of the SMAs are consistent but slightly bimodal, and we found that adding the host and companion RVs moved our SMAs toward the lower valley $\sim$15 au. The eccentricity is not well constrained, with its posteriors consistent with a wide range (0.0–0.6 within 95% confidence intervals) due to the sparse orbital coverage. The posteriors of the parallaxes are consistent with our Gaussian priors, and as described are significantly different ($\sim 3.6\sigma$) compared to the Gaia DR2 parallax (37.6462 ± 0.0643 mas) used in Currie et al. (2020). The posteriors of the inclinations and primary masses of our HGCA fit and relative astrometry with primary and companion RVs are consistent with the Currie et al. (2020) measurements, which are reasonable given that we started with the same mass priors as in Currie et al. (2020). However, we found that the primary and companion masses from our Gaia Hipparcos IAD fits are significantly different than our other settings, due to the aforementioned underestimated Hipparcos IAD uncertainties. For the companion masses, the posteriors are consistent with our HGCA fits and the Currie et al. (2020) measurements. The fits with relative astrometry and RVs are unable to constrain the companion masses well because the mass and SMA measurements are more sensitive to orbit phase coverage from the absolute astrometry. We, therefore, adopted the HGCA fit with both primary and companion RVs as it has all of the information available and is consistent with the literature values from Currie et al. (2020).

7. Placing HD 33632 Ab to the Rotational Demographics of Very Low-mass Objects

In this section, we compare our measured $v \sin i$ of HD 33632 Ab to the population of the VLM objects reported in the literature, by comparing its $v \sin i$ against spectral type, and by rotational velocity against mass.

7.1. Overall Projected Rotational Velocity Distribution

The rotational evolution of VLM objects ($M < 0.1$ $M_\odot$) has been examined in several studies, for the ultracool dwarf ($T_{\rm eff} \leqslant 3000$ K; spectral type of M6 or later; Kirkpatrick 2005) regime (Zapatero Osorio et al. 2006; Radigan et al. 2012; Metchev et al. 2015; Prato et al. 2015; Vos et al. 2017, 2018, 2019; Hsu et al. 2021; Popinchalk et al. 2021; Hsu et al. 2024) and for low-mass companions and gas giant exoplanets (Bryan et al. 2018, 2020; Xuan et al. 2020; Wang et al. 2021).

Figure 8 illustrates the current consensus of $v \sin i$ distribution versus spectral type for VLM objects, ranging from M5 to T9. The $v \sin i$ sample has 457 objects, compiled from Crossfield (2014), Hsu et al. (2021), Tannock et al. (2021), and Hsu et al. (2024). These high-resolution spectroscopic measurements are limited at $v \sin i \sim 5$–9 km s^{-1} for mid-M to T dwarfs. The overall increase of $v \sin i$ toward later spectral types can be explained by the spin-up mechanism under constant angular momentum evolution (Zapatero Osorio et al. 2006; Hsu et al. 2021). HD 33632 Ab, while being a relatively fast rotator ($v \sin i = 53 \pm 3$ km s^{-1}), falls within the $v \sin i$ trend of the L dwarfs. Interestingly, HD 4747 B, an L9.5 object, has a much lower $v \sin i$ ($13.2^{+1.4}_{-1.5}$ km s^{-1}; Xuan et al. 2022) and methane detection, compared to HD 33632 Ab of the same spectral type.

7.2. Comparison of Rotation with Mass

Our comparisons of the projected rotational velocity versus spectral type suffer from observational degeneracy between age and mass. To possibly break this degeneracy, we attempted to parameterize the spin, evolved to the same age, versus mass, which might show evidence of a mass-dependent trend with rotation (Batygin 2018; Ginzburg & Chiang 2020).

We examined the companion spins versus the masses of known low-mass companions ($M < 0.1$ $M_\odot$), gas giant exoplanets, and solar system planets, following the analysis outlined in Wang et al. (2021). The spins are parameterized as the rotational velocity over the breakup velocity. Our prescription is detailed as follows. We constructed a sample that has $v \sin i$ or rotational period measurements for companions, free-floating VLM objects, and solar system

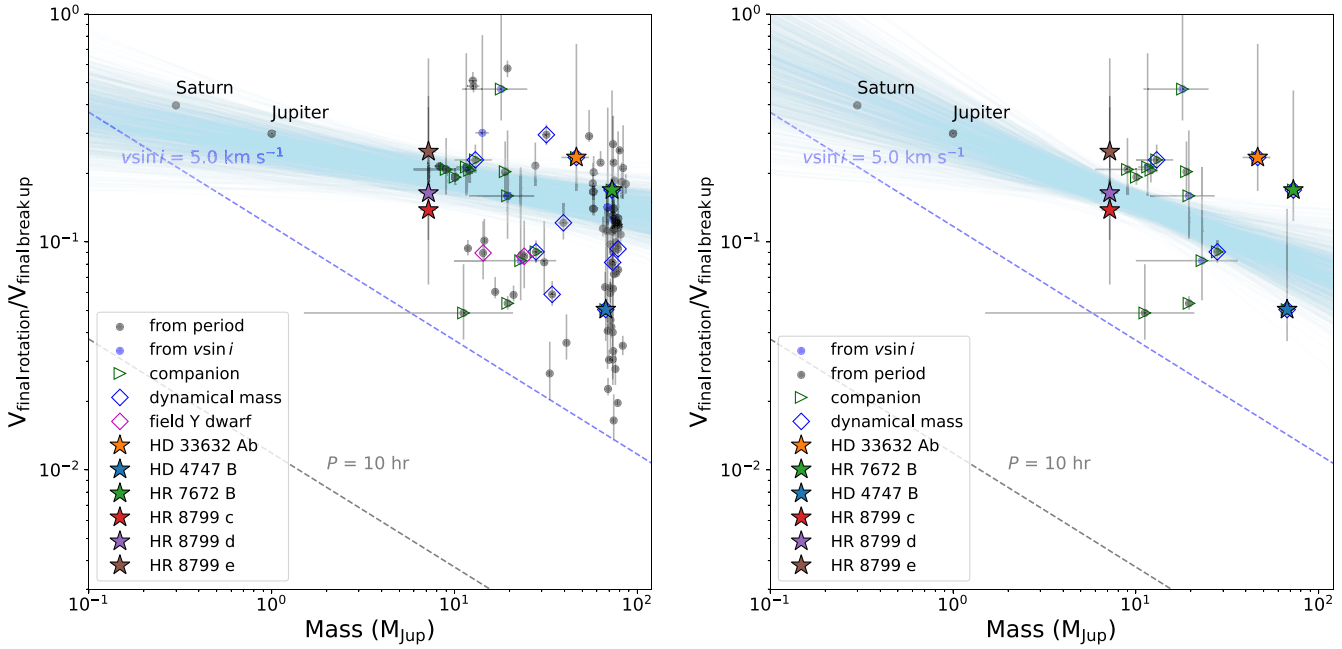

Figure 9. Companion spin vs. mass for known low-mass companions ($M < 0.1\ M_{\odot}$) and solar system planets. The spins are parameterized as the final rotational velocity over the final breakup velocity under constant angular momentum evolution to 5 Gyr. Left: final spin vs. mass for all objects in our spin sample, including free-floating field objects, low-mass companions, and solar system planets. The sample is compiled from literature $v \sin i$ (blue dots) and rotational period (gray dots) measurements. The known companions and dynamical mass measurements are labeled in green triangles and blue diamonds, respectively. Spin measurements published with KPIC are labeled in star symbols. The detection limits for $v \sin i$ (<5 km s^{-1}) and photometry time series (>10 hr) are plotted in blue and gray dashed lines, respectively. The random draws of 1000 solutions from the best-fit rotational trend from Wang et al. (2021) are depicted in light blue lines. Right: final spin vs. mass for the companions in our spin sample, including the low-mass companions and solar system planets. The rest is the same as the left panel.

planets (i.e., Jupiter and Saturn). Our VLM rotational sample is mostly constructed from Bryan et al. (2020), Hsu et al. (2021), Popinchalk et al. (2021), Tannock et al. (2021), Wang et al. (2021), Vos et al. (2022), and Hsu et al. (2024), for a total of 237 objects. Among these catalogs, the majority of the sources lack direct mass measurements, so we crossmatched with the Two Micron All-Sky Survey catalog (Cutri et al. 2003) to obtain their H-band magnitudes and parallaxes from Gaia DR3 (Gaia Collaboration et al. 2023). Using absolute magnitudes and reasonable assumptions of their ages, their mass and radii can be inferred from interpolation of theoretical VLM evolutionary models (Baraffe et al. 2003). Next, we need to convert these measurements into rotational velocities. There are two types of spins in our sample, including $v \sin i$ and rotational periods (P) from the photometric time series. For $v \sin i$, the geometric sine distribution is assumed to compute the rotational velocities. For rotational periods, radii are needed to infer the rotational velocities. We used the Baraffe et al. (2003) models with age and another parameter to linearly interpolate and infer the model radius, which includes the mass (preferred), or absolute H-band magnitude. We first use the dynamical masses, then the literature masses, and then the absolute H-band magnitude. For ages, those of known clusters are used (Gagné et al. 2018b; sampled as uniform distributions within their 1σ uncertainties), or a field age is assumed otherwise (sampled as a uniform distribution between 0.5 and 10 Gyr). We also removed sources younger than 10 Myr to avoid possible disk interaction that slows down the spin and biases our analysis. Using these inferred parameters (age, mass, and radius), we can compute their rotational velocities and breakup velocities. The breakup velocity is defined as $v_{\rm breakup} = \sqrt{\frac{GM}{R}}$, where mass M and radius R are derived from the Baraffe et al. (2003) evolutionary models, and G is the gravitational constant. Finally, to minimize the age effect on our analysis, we computed their "final" rotational velocities and "final" breakup velocities by evolving their rotation to 5 Gyr assuming conservation of angular momentum. For the derived parameters, the associated uncertainties were propagated using the Monte Carlo method with 1000 draws.

Figure 9 shows the "final" rotational velocities and "final" breakup velocities against the masses of our sample. We overplotted the best-fit parameters for the mass versus rotation trend from Wang et al. (2021) on top of our final sample. In particular, the final rotational velocity and final breakup velocity of HD 33632 Ab are 73^{+153}_{-20} km s^{-1} and 315^{+26}_{-27} km s^{-1}, respectively. The ratio of these two gives the final rotational velocity over the breakup velocity of $0.23^{+0.50}_{-0.07}$, well below the breakup velocity and following the population trend with the parameters in Bryan et al. (2020) and Wang et al. (2021). The larger upper uncertainty highlights the inclination effect, while the more constrained lower uncertainty is partially constrained by our relatively high $v \sin i$. HR 7672 B, another relatively fast rotator, follows a similar trend, with its final velocity over breakup velocity being $0.17^{+0.29}_{-0.05}$. HD 4747 B, on the other hand, has a much lower final velocity over breakup velocity of $0.050^{+0.089}_{-0.013}$, due to its lower $v \sin i$ of 13.2 ± 1.5 km s^{-1}. For the HR 8799 cde planets, their masses and $v \sin i$ values are similar (8.1 ± 4 km s^{-1}, 10.1 ± 2.8 km s^{-1}, and 15 ± 2.6 km s^{-1}, respectively), resulting in similar final velocity over breakup velocity ratios of $0.14^{+0.25}_{-0.07}$, $0.16^{+0.27}_{-0.06}$, and $0.25^{+0.39}_{-0.08}$, respectively. As pointed out in Wang et al. (2021), there seems to be no clear trend for rotation versus mass for free-floating objects (left panel of Figure 9), while there is a tentative trend for companions and solar system planets (right panel of Figure 9). However, toward the VLM end, only two solar system planets, Jupiter and Saturn, provide measurements below 5 $M_{\rm Jup}$, and current ground and space instruments are unavailable to provide

any rotation in this regime. Future observations with young companions such as AF Lep b (De Rosa et al. 2023; Franson et al. 2023; Mesa et al. 2023; Zhang et al. 2023; ∼3–5 $M_{\rm Jup}$) as well as the discovery of additional planetary-mass objects below the deuterium burning mass limit will help us critically examine this trend. Even for masses between 5 and 100 $M_{\rm Jup}$, the sample size is still too small, and more rotation measurements for VLM objects in this range are needed with instruments such as KPIC.

8. Summary

We present Keck/KPIC high-resolution *K*-band spectroscopy of the benchmark brown dwarf mass companion HD 33632 Ab, which provided companion radial and projected rotational velocities as well as CO and H_2O abundances. Our main findings are as follows.

1. HD 33632 Ab's projected rotational velocity ($v \sin i$) and RV measurements are 53 ± 3 km s^{-1} and -8 ± 3 km s^{-1}, respectively, using a forward-modeling framework that incorporates host star spectra and self-consistent substellar atmospheric models from the BT-Settl (Allard et al. 2012) and Sonora–Bobcat models (Marley et al. 2021). Our $v \sin i$ and RV values are consistent across different assumptions of clear versus cloudy models.
2. Using our measured relative RV, updated Gaia parallax, and HGCA (Brandt 2021), we measured the updated orbital solutions with the `orbitize!` package. Our measured companion mass $m_2 = 37^{+7}_{-4}$ $M_{\rm Jup}$, eccentricity $e = 0.25^{+0.17}_{-0.18}$, period $P = 74^{+34}_{-16}$ yr, and mass ratio q $(m_2/m_1) = 0.032^{+0.006}_{-0.004}$ are consistent with the measurements in Currie et al. (2020).
3. Carbon monoxide and water vapor are clearly detected in our Keck/KPIC spectra of HD 33632 Ab, both with the cross-correlation approach and the forward-retrieval method that utilizes on-axis host star spectra as an empirical star flux model, and substellar molecular templates as the companion models. Using the forward-retrieval framework with the `petitRADTRANS` package under 24 model assumptions, the mass fractions of logCO and logH_2O are found to be -2.3 ± 0.3 and -2.7 ± 0.2, respectively (or volume mixing ratios of -3.34 ± 0.18 and $-3.54^{+0.17}_{-0.18}$, respectively).
4. While methane is possibly present in L–T transition objects, we did not detect methane in our Keck/KPIC spectra of HD 33632 Ab, using the cross-correlation method against methane molecular templates or forward-retrieval models. This could be due to several factors, including the relatively low S/N of our KPIC spectra, the fast rotation of HD 33632 Ab, disequilibrium chemistry, and possible earlier spectral type than L9.5 previously reported.
5. Our inferred metallicity ([C/H] $= 0.0 \pm 0.2$ dex) and C/O ratio (0.58 ± 0.14) are consistent with the host star metallicity ([C/H] $= -0.13 \pm 0.05$ and [Fe/H] $= -0.15 \pm 0.03$) as well as its C/O ratio ($0.39^{+0.12}_{-0.09}$) within 1.5σ, expected for brown dwarf companions formed through gravitational core collapse or disk instability.
6. HD 33632 Ab is a relatively fast rotator but follows the general trend of brown dwarf rotational demographics. We compared the rotation of HD 33632 Ab with literature spin measurements, including $v \sin i$ and photometric periods of 237 low-mass stars, brown dwarfs and directly imaged exoplanets. Assuming uniform distributions of inclination for a population of field and companion low-mass stars, brown dwarfs, and directly imaged exoplanets, we inferred the ratio of the rotation velocity over the breakup velocity ("final" $v/v_{\rm break}$) at an age of 5 Gyr assuming constant angular momentum evolution. We examined if angular momenta for lower-mass companions is lost less due to weakened magnetic interactions in protoplanetary/stellar disks (Batygin 2018; Ginzburg & Chiang 2020). We found a tentative trend with a yet small sample size of 21 sources, similar to the findings in Bryan et al. (2020) and Wang et al. (2021).

Future observations of relative and absolute astrometry, as well as parallax for HD 33632 Ab (e.g., Gaia Data Release 4), will provide a longer and more precise orbital phase coverage to improve the orbital solution. In the meantime, more advanced speckle nulling methods for KPIC (Xin et al. 2023), fringing modeling, more sophisticated forward/retrieval modeling (Xuan et al. 2024), as well as new hardware upgrades in 2024 will allow us to increase the sensitivity of detection and enable more precise measurements of radial and projected rotational velocities, and abundances. Current instrument and modeling capabilities, including Keck/KPIC, VLT/CRIRES+ (Follert et al. 2014), VLT/HiRISE (Otten et al. 2021), and Subaru/REACH (Kotani et al. 2020) will significantly increase the sample of the spins and abundances for dozens of directly imaged brown dwarf companions and exoplanets, while next-generation high-resolution spectrographs such as Keck/HISPEC, TMT/MODHIS (Mawet et al. 2022; Konopacky et al. 2023), and ELT/ANDES (Marconi et al. 2022) will significantly expand the current rotation and abundances for low-mass companions and directly imaged exoplanets.

Acknowledgments

The authors thank the anonymous referees for their useful comments, which improved the original manuscript. The authors thank Trent Dupuy for providing useful comments, which have improved this manuscript. The authors thank the Keck observing assistants Heather Hershley, Arina Rostopchina, and Tony Connors and support astronomer Carlos Alvarez for their help in obtaining the Keck/KPIC spectra. J.X. acknowledges support from the NASA Future Investigators in NASA Earth and Space Science and Technology (FINESST) award #80NSSC23K1434. This research was supported in part through the computational resources and staff contributions provided for the Quest high-performance computing facility at Northwestern University, which is jointly supported by the Office of the Provost, the Office for Research, and Northwestern University Information Technology. This work used computing resources provided by Northwestern University and the Center for Interdisciplinary Exploration and Research in Astrophysics (CIERA). Funding for KPIC has been provided by the California Institute of Technology, the Jet Propulsion Laboratory, the Heising-Simons Foundation (grants #2015-129, #2017-318, #2019-1312, and #2023-4598), the Simons Foundation (through the Caltech Center for Comparative Planetary Evolution), and the NSF under grant AST-1611623. Data presented herein were obtained at the W. M. Keck Observatory, which is operated as a scientific partnership among the California Institute of Technology, the University of California, and the National Aeronautics and Space Administration. The Observatory was made possible by the generous financial support of the W. M. Keck Foundation. The authors recognize and acknowledge the significant

cultural role and reverence that the summit of Maunakea has with the indigenous Hawaiian community, and that the W. M. Keck Observatory stands on Crown and Government Lands that the State of Hawai'i is obligated to protect and preserve for future generations of indigenous Hawaiians.

Facilities: Keck:II (NIRSPEC) and Keck:II (NIRC2).

Software: `Astropy` (Astropy Collaboration et al. 2013, 2018), `Numpy` (Harris et al. 2020), `Scipy` (Virtanen et al. 2020), `Matplotlib` (Hunter 2007), `DYNESTY` (Speagle 2020), `orbitize!` (Blunt et al. 2020), `emcee` (Foreman-Mackey et al. 2013), `seaborn` (Waskom 2021), and `SMART` (Hsu et al. 2021, 2021).

Appendix A
Forward-modeling Best-fit Results

We present the remaining best-fit models and posterior probability distributions using the forward-modeling and forward-retrieval modeling methods presented in Sections 4 and 5. We show the residual companion spectra after removal of the modeled star flux in Figure A1, the best-fit forward-model using the Sonora models in Figure A2, and the best-fit forward-retrieval model and its posterior probability distributions in Figure A3 and Figure A4, respectively.

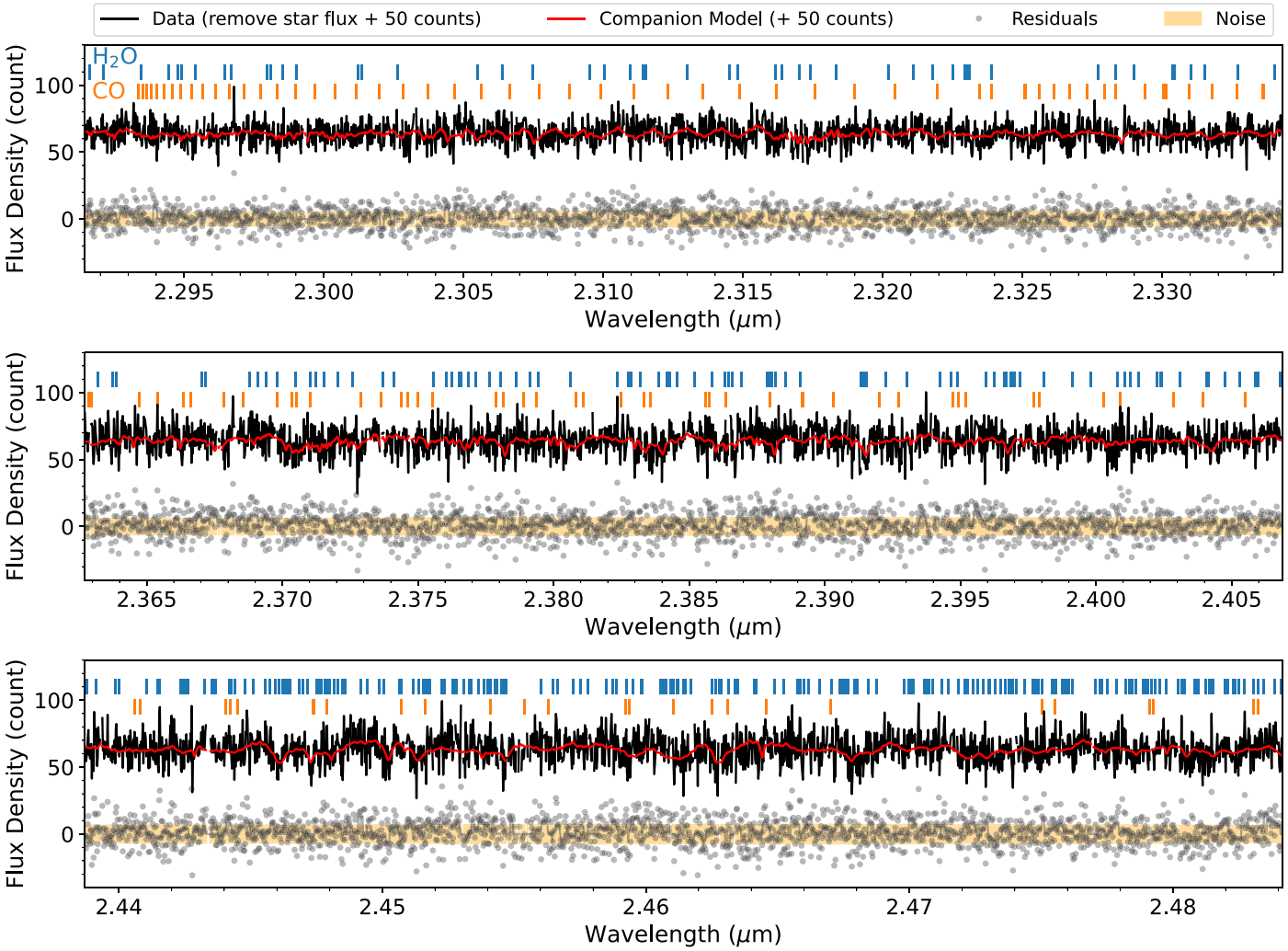

Figure A1. The residual companion spectra after removal of the modeled star flux in Figure 2. The companion spectra (black lines) and companion model (red lines) have been shifted by 50 counts for better visualization. The data noise (light yellow shaded regions) and residuals (gray dots) are depicted. The CO and H_2O features are labeled by the vertical orange and light blue lines, respectively.

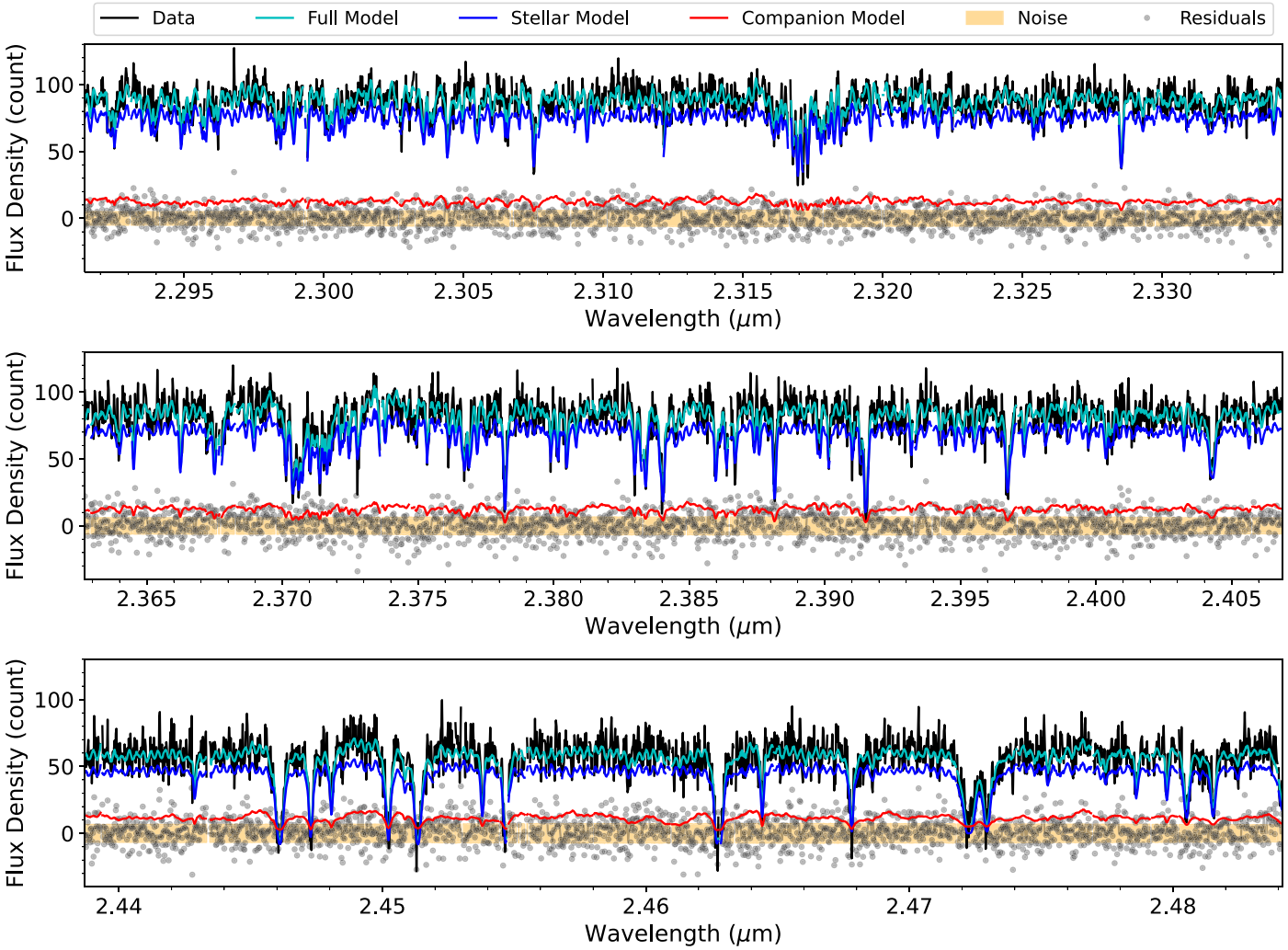

Figure A2. Same as Figure 2 using the Sonora models.

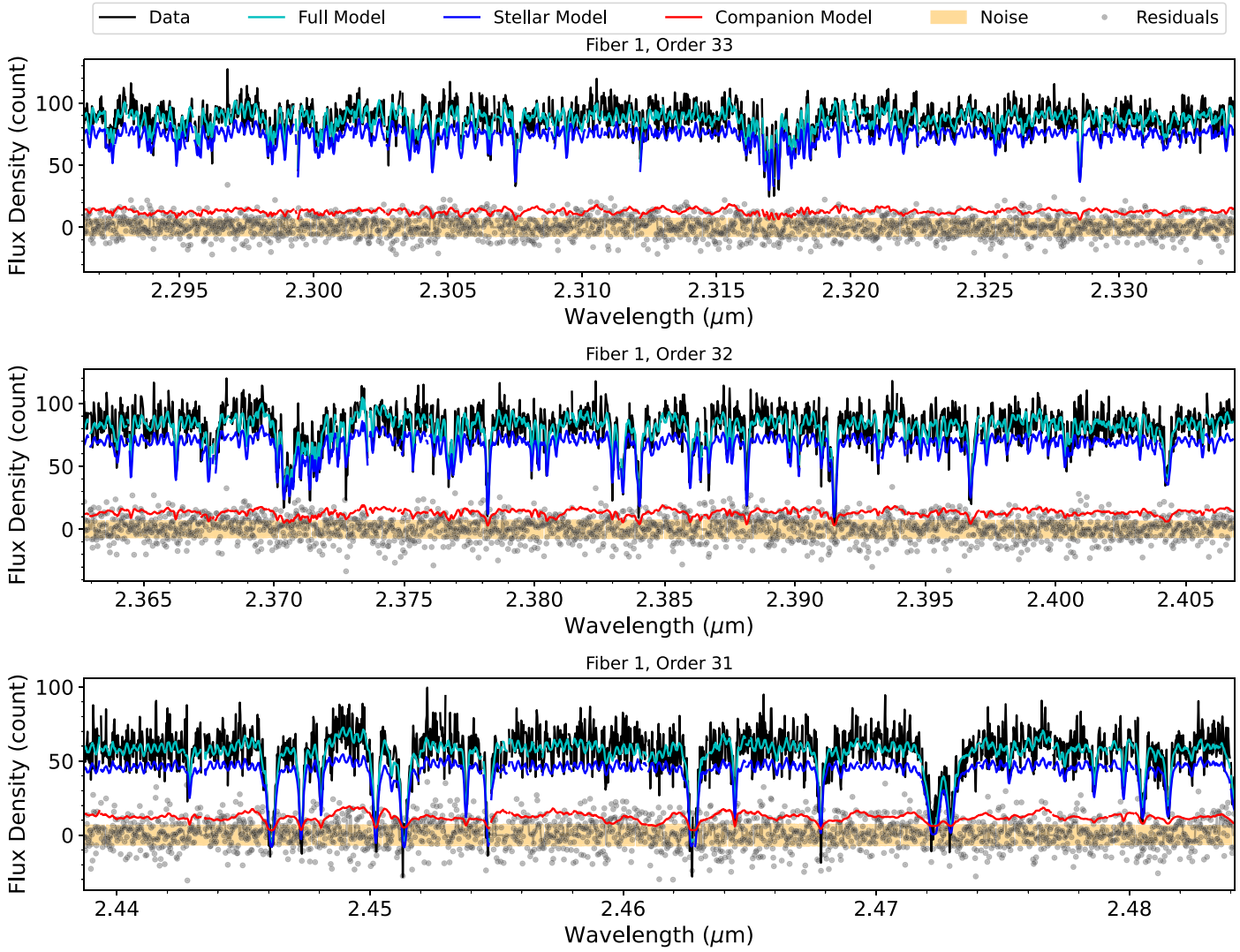

Figure A3. The best-fit baseline forward-retrieval model and fiber 1 spectrum of HD 33632 Ab. The labels are identical to Figure 2.

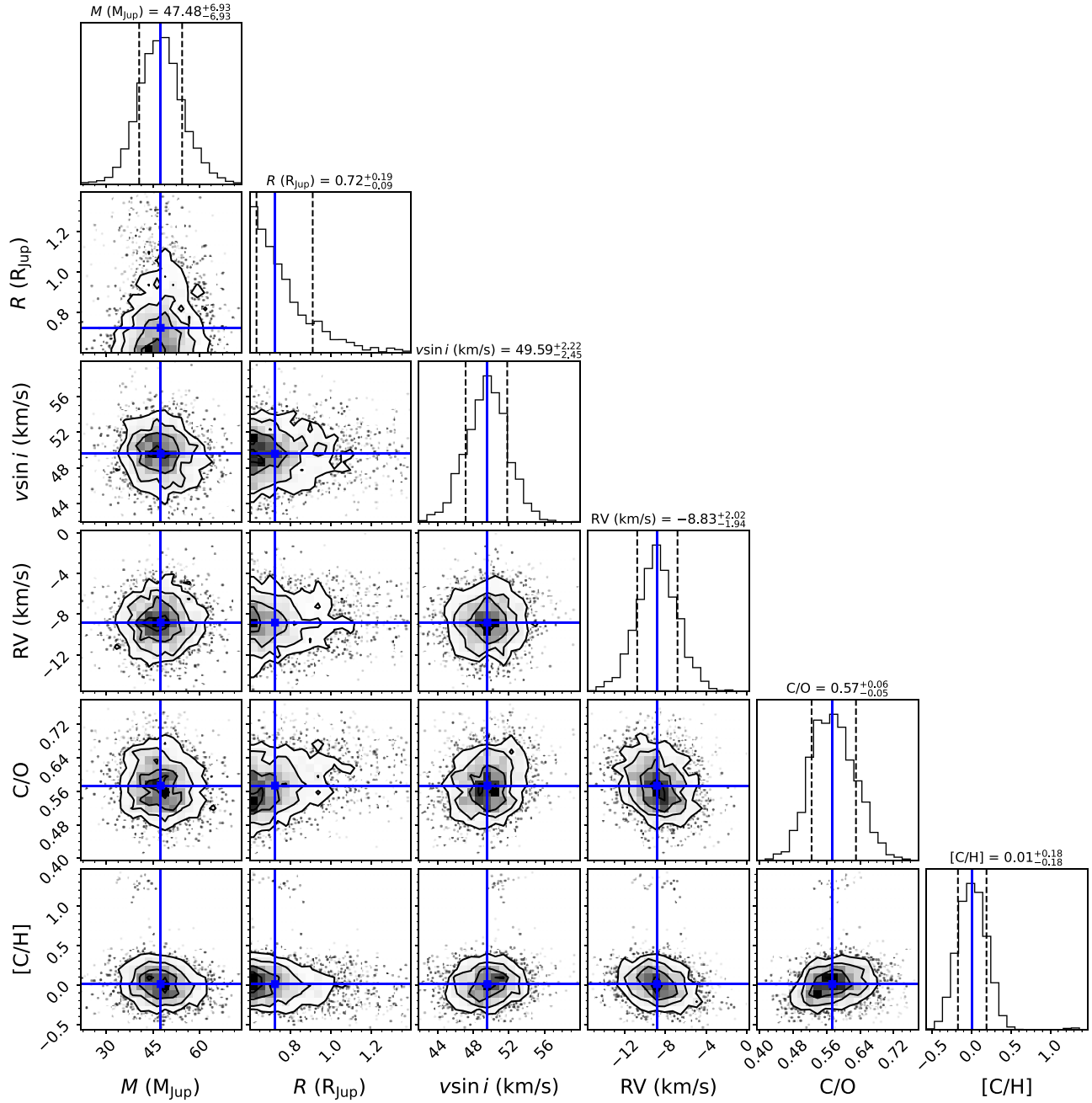

Figure A4. Posterior probability distributions of our baseline forward-retrieval model of HD 33632 Ab for the selected substellar parameters. The median values are labeled in blue lines, and the 16th and 84th percentiles are labeled in black dashed lines.

Appendix B
Orbital Fitting

In Section 6, we presented the refined orbital solutions using our relative RV, Gaia EDR3 astrometry, and the updated HGCA (Brandt 2021). Here we present the best-fit orbits in Figure B1 and the associated orbital diagnostics in Figure B2 and a summary table in Table B1 under various assumptions.

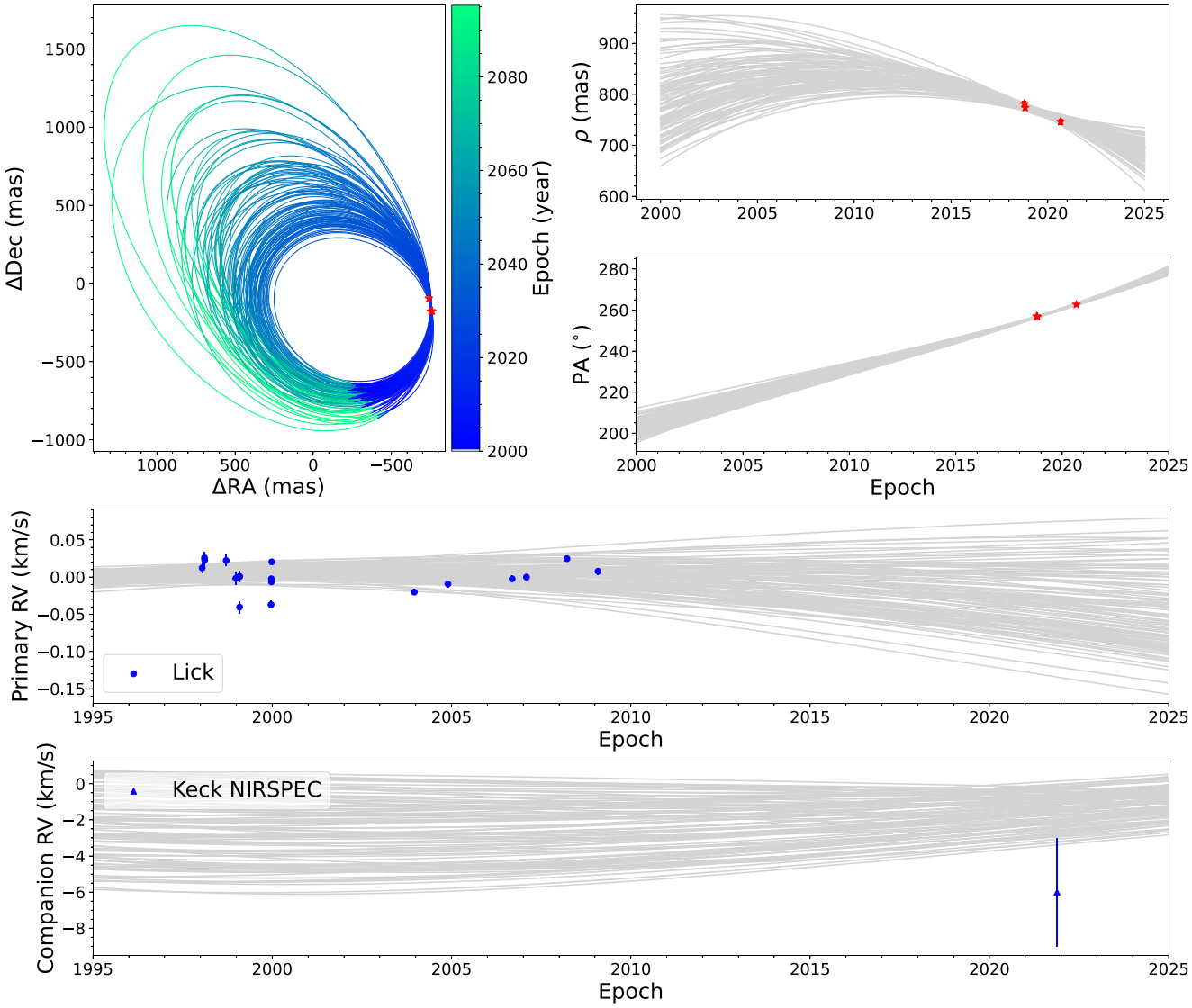

Figure B1. Best-fit 100 random draw orbits for HD 33632 Ab, using host and companion RVs and the HGCA (EDR3) (Brandt 2021) with the `orbitize!` package. Upper left: best-fit orbits in ΔR.A. and Δdecl. coordinates for the HD 33632 Ab system (blue–green lines) and the relative astrometry (red stars) from Currie et al. (2020). Upper right, top: best-fit separation (ρ) in mas (gray lines) with the relative astrometry (red stars) from Currie et al. (2020). Upper right, bottom: best-fit PAs in degrees (gray lines) with the relative astrometry (red stars) from Currie et al. (2020). Middle: best-fit RV orbits (gray lines) for the host star HD 33632 A using the Lick measurements (blue dots). Bottom: best-fit RV orbits (gray lines) for the companion HD 33632 Ab using our Keck/KPIC measurements (blue triangle). See Section 6 for details.

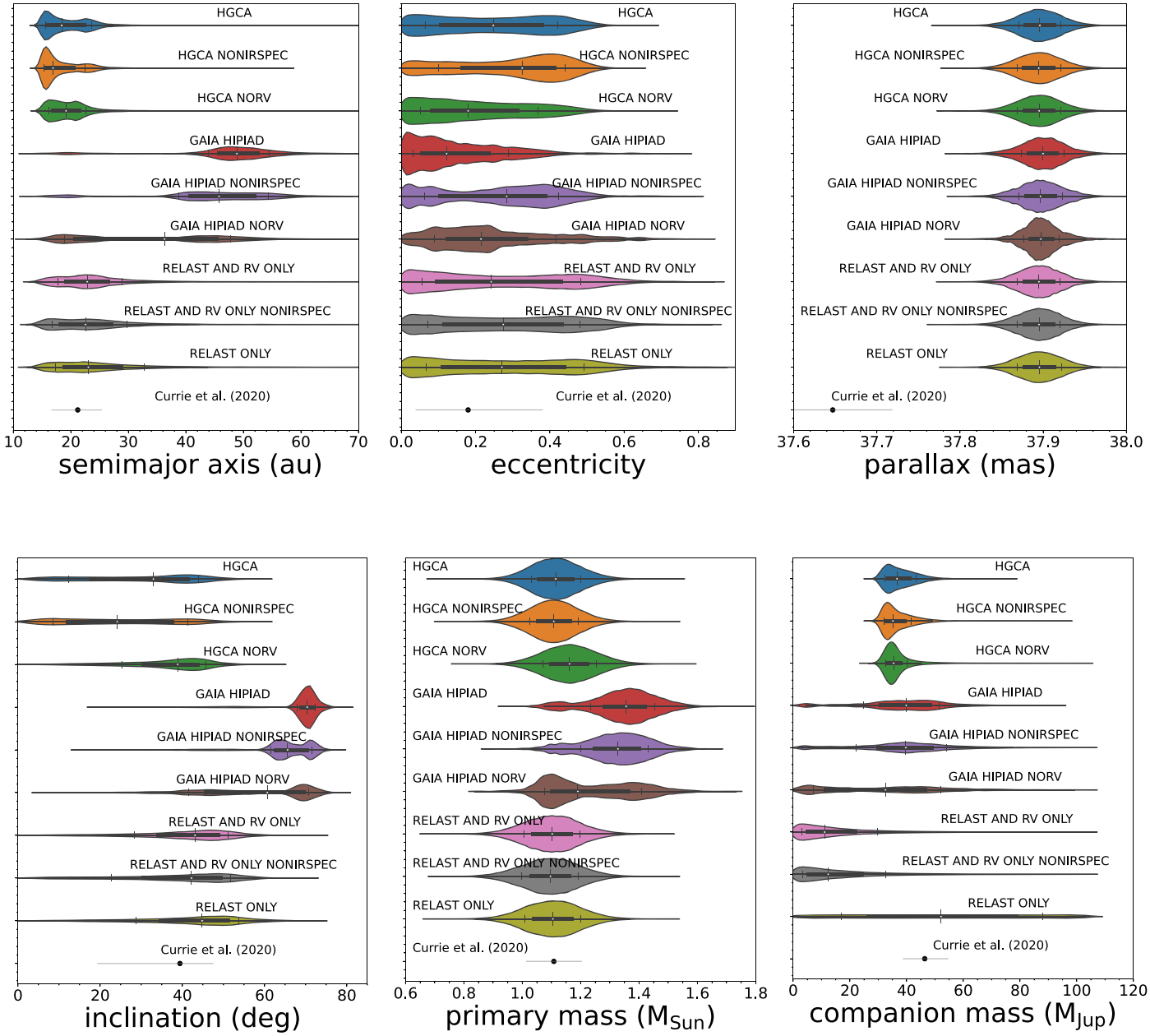

Figure B2. Violin plots of the best-fit orbital parameters. Top left: SMA (au). Top middle: eccentricity. Top right: parallax (mas). Bottom left: inclination (degrees). Bottom middle: primary mass ($M_{\odot}$). Bottom right: secondary mass (M_J). Each panel, from top to bottom, illustrates (1–3): the joint orbit fit using the EDR3 edition of the HGCA (Brandt 2021); (4–6) the joint orbit fit using Gaia and Hipparcos IAD from van Leeuwen (2007); (7–9) using relative astrometry measurements in Currie et al. (2020); and (10) the orbital solutions in Currie et al. (2020). Under each scenario, we consider three combinations: (1) one with both primary (Lick) and secondary (NIRSPEC) RVs, (2) one with only the primary (Lick) RVs, and (3) one without RVs. The major difference is due to the updated Gaia EDR3 version of HGCA and Gaia DR3 parallaxes compared to earlier solutions illustrated in Currie et al. (2020).

Table B1
HD 33632 Ab Best-fit Orbital Parameters

Parameter	HGCA			Gaia and Hipparcos IAD			Relative Astrometry Only			Prior[a]	Currie2020
	All RVs	No RV_2	No RVs	All RVs	No RV_2	No RVs	All RVs	No RV_2	No RVs		
					Fitted Parameters						
a (au)	18^{+5}_{-3}	17^{+6}_{-2}	19^{+4}_{-3}	49^{+6}_{-5}	46^{+9}_{-7}	36^{+12}_{-17}	23^{+6}_{-5}	23^{+7}_{-6}	23^{+10}_{-6}	$\mathcal{U}$(0.001, 10000)	$21.2^{+4.1}_{-4.5}$
e	$0.25^{+0.17}_{-0.18}$	$0.33^{+0.12}_{-0.22}$	$0.18^{+0.19}_{-0.13}$	$0.12^{+0.17}_{-0.09}$	$0.28^{+0.14}_{-0.22}$	$0.21^{+0.2}_{-0.12}$	$0.24^{+0.24}_{-0.19}$	$0.27^{+0.21}_{-0.2}$	$0.27^{+0.22}_{-0.2}$	$\mathcal{U}$(0,1)	$0.18^{+0.20}_{-0.14}$
i (deg)	33^{+11}_{-21}	24^{+17}_{-16}	39^{+7}_{-14}	70^{+2}_{-2}	66^{+6}_{-4}	61^{+10}_{-19}	43^{+8}_{-15}	42^{+10}_{-20}	45^{+9}_{-16}	$\mathcal{U}$(sine)	39^{+8}_{-20}
π (mas)	$37.9^{+0.03}_{-0.03}$	$37.89^{+0.03}_{-0.03}$	$37.9^{+0.03}_{-0.03}$	$37.9^{+0.03}_{-0.03}$	$37.9^{+0.03}_{-0.03}$	$37.9^{+0.02}_{-0.02}$	$37.89^{+0.03}_{-0.03}$	$37.9^{+0.03}_{-0.03}$	$37.9^{+0.03}_{-0.03}$	$\mathcal{N}$(37.8953, 0.026)	37.647 ± 0.071
ω (deg)	65^{+248}_{-47}	47^{+265}_{-30}	134^{+202}_{-113}	105^{+125}_{-26}	203^{+18}_{-106}	93^{+188}_{-39}	233^{+80}_{-194}	219^{+97}_{-194}	225^{+89}_{-191}	$\mathcal{U}$(0, π)	151^{+155}_{-131}
Ω (deg)	39^{+21}_{-9}	38^{+38}_{-11}	54^{+17}_{-17}	21^{+148}_{-6}	175^{+4}_{-157}	30^{+64}_{-13}	51^{+64}_{-18}	43^{+68}_{-19}	47^{+63}_{-27}	$\mathcal{U}$(0, 2π)	38 ± 7
τ	$0.37^{+0.29}_{-0.05}$	$0.35^{+0.15}_{-0.03}$	$0.4^{+0.3}_{-0.08}$	$0.53^{+0.08}_{-0.17}$	$0.25^{+0.29}_{-0.06}$	$0.4^{+0.13}_{-0.22}$	$0.29^{+0.41}_{-0.16}$	$0.3^{+0.24}_{-0.15}$	$0.3^{+0.38}_{-0.17}$	$\mathcal{U}$(0, 1)	$0.48^{+0.2}_{-0.23}$
m_1 (M_J)	37^{+7}_{-4}	35^{+7}_{-3}	35^{+5}_{-3}	40^{+12}_{-15}	40^{+14}_{-18}	33^{+20}_{-26}	11^{+19}_{-8}	12^{+20}_{-9}	52^{+36}_{-35}	$\mathcal{U}$(0, 0.1) $M_\odot$	$46.4^{+8.1}_{-7.5}$
m_0 ($M_\odot$)	$1.11^{+0.09}_{-0.08}$	$1.11^{+0.08}_{-0.08}$	$1.16^{+0.09}_{-0.09}$	$1.36^{+0.1}_{-0.12}$	$1.33^{+0.1}_{-0.13}$	$1.19^{+0.22}_{-0.11}$	$1.1^{+0.09}_{-0.1}$	$1.1^{+0.1}_{-0.1}$	$1.1^{+0.09}_{-0.1}$	$\mathcal{N}$(1.11, 0.09)	1.11 ± 0.09
					Derived Parameters						
P (yr)	74^{+34}_{-16}	66^{+34}_{-10}	77^{+23}_{-17}	289^{+51}_{-44}	266^{+72}_{-59}	196^{+82}_{-119}	104^{+44}_{-33}	102^{+52}_{-36}	103^{+72}_{-36}		91 ± 27
m_1/m_0	$0.032^{+0.006}_{-0.004}$	$0.031^{+0.006}_{-0.003}$	$0.029^{+0.005}_{-0.003}$	$0.028^{+0.008}_{-0.011}$	$0.028^{+0.011}_{-0.012}$	$0.024^{+0.014}_{-0.018}$	$0.01^{+0.017}_{-0.007}$	$0.011^{+0.018}_{-0.008}$	$0.045^{+0.031}_{-0.03}$		$0.0402^{+0.0078}_{-0.0073}$

Notes.
[a] $\mathcal{U}$ and $\mathcal{N}$ stand for uniform and normal priors, respectively.
[b] Sampled in log space.
[c] Derived from the periastron time in Currie et al. (2020).

ORCID iDs

Chih-Chun Hsu https://orcid.org/0000-0002-5370-7494
Jason J. Wang (王劲飞) https://orcid.org/0000-0003-0774-6502
Jerry W. Xuan https://orcid.org/0000-0002-6618-1137
Jean-Baptiste Ruffio https://orcid.org/0000-0003-2233-4821
Evan Morris https://orcid.org/0000-0003-3165-0922
Daniel Echeverri https://orcid.org/0000-0002-1583-2040
Yinzi Xin https://orcid.org/0000-0002-6171-9081
Joshua Liberman https://orcid.org/0000-0002-4934-3042
Luke Finnerty https://orcid.org/0000-0002-1392-0768
Katelyn Horstman https://orcid.org/0000-0001-9708-8667
Ben Sappey https://orcid.org/0000-0003-1399-3593
Dimitri Mawet https://orcid.org/0000-0002-8895-4735
Nemanja Jovanovic https://orcid.org/0000-0001-5213-6207
Michael P. Fitzgerald https://orcid.org/0000-0002-0176-8973
Jacques-Robert Delorme https://orcid.org/0000-0001-8953-1008
J. Kent Wallace https://orcid.org/0000-0001-5299-6899
Ashley Baker https://orcid.org/0000-0002-6525-7013
Geoffrey A. Blake https://orcid.org/0000-0003-0787-1610
Benjamin Calvin https://orcid.org/0000-0003-4737-5486
Ronald A. López https://orcid.org/0000-0002-2019-4995
Andrew Skemer https://orcid.org/0000-0001-6098-3924
Ji Wang https://orcid.org/0000-0002-4361-8885

References

Ackerman, A. S., & Marley, M. S. 2001, ApJ, 556, 872
Adams, A. D., Meyer, M. R., Howe, A. R., et al. 2023, AJ, 166, 192
Allard, F., Homeier, D., & Freytag, B. 2012, RSPTA, 370, 2765
Ammons, S. M., Robinson, S. E., Strader, J., et al. 2006, ApJ, 638, 1004
Anderson, E., & Francis, C. 2012, AstL, 38, 331
Asplund, M., Grevesse, N., Sauval, A. J., & Scott, P. 2009, ARA&A, 47, 481
Astropy Collaboration, Price-Whelan, A. M., Sipőcz, B. M., et al. 2018, AJ, 156, 123
Astropy Collaboration, Robitaille, T. P., Tollerud, J. E., et al. 2013, A&A, 558, A33
Baraffe, I., Chabrier, G., Barman, T. S., Allard, F., & Hauschildt, P. H. 2003, A&A, 402, 701
Bate, M. R., & Bonnell, I. A. 2005, MNRAS, 356, 1201
Batygin, K. 2018, AJ, 155, 178
Blake, C. H., Charbonneau, D., & White, R. J. 2010, ApJ, 723, 684
Blunt, S., Wang, J. J., Angelo, I., et al. 2020, AJ, 159, 89
Brandt, T. D. 2021, ApJS, 254, 42
Bryan, M. L., Benneke, B., Knutson, H. A., Batygin, K., & Bowler, B. P. 2018, NatAs, 2, 138
Bryan, M. L., Ginzburg, S., Chiang, E., et al. 2020, ApJ, 905, 37
Burgasser, A. J., Blake, C. H., Gelino, C. R., Sahlmann, J., & Bardalez Gagliuffi, D. 2016, ApJ, 827, 25
Burningham, B., Faherty, J. K., Gonzales, E. C., et al. 2021, MNRAS, 506, 1944
Burningham, B., Marley, M. S., Line, M. R., et al. 2017, MNRAS, 470, 1177
Burrows, A., Hubbard, W. B., Lunine, J. I., & Liebert, J. 2001, RvMP, 73, 719
Burrows, A., Marley, M., Hubbard, W. B., et al. 1997, ApJ, 491, 856
Calamari, E., Faherty, J. K., Visscher, C., et al. 2024, ApJ, 963, 67
Casagrande, L., Schönrich, R., Asplund, M., et al. 2011, A&A, 530, A138
Chan, Y. M., & Dalgarno, A. 1965, PPS, 85, 227
Chen, Y. Q., Nissen, P. E., Zhao, G., Zhang, H. W., & Benoni, T. 2000, A&AS, 141, 491
Crossfield, I. J. M. 2014, A&A, 566, A130
Curiel, S., Ortiz-León, G. N., Mioduszewski, A. J., & Torres, R. M. 2020, AJ, 160, 97
Currie, T., Biller, B., Lagrange, A., et al. 2023, in ASP Conf. Ser. 534, Protostars and Planets VII, ed. S. Inutsuka et al. (San Francisco, CA: ASP), 799
Currie, T., Brandt, T. D., Kuzuhara, M., et al. 2020, ApJL, 904, L25
Cutri, R. M., Skrutskie, M. F., van Dyk, S., et al. 2003, 2MASS All Sky Catalog of point sources, NASA/IPAC Infrared Science Archive, http://irsa.ipac.caltech.edu/applications/Gator/
Dalgarno, A., & Williams, D. A. 1962, ApJ, 136, 690
de Bruijne, J. H. J., & Eilers, A. C. 2012, A&A, 546, A61
De Rosa, R. J., Nielsen, E. L., Wahhaj, Z., et al. 2023, A&A, 672, A94
Del Burgo, C., Martín, E. L., Zapatero Osorio, M. R., & Hauschildt, P. H. 2009, A&A, 501, 1059
Delorme, J.-R., Jovanovic, N., Echeverri, D., et al. 2021, JATIS, 7, 035006
ESA Special Publication 1997, The HIPPARCOS and TYCHO catalogues, Vol. 1200 Astrometric and photometric star catalogues derived from the ESA HIPPARCOS Space Astrometry Mission
Faherty, J. K., Gagné, J., Popinchalk, M., et al. 2021, ApJ, 923, 48
Filippazzo, J. C., Rice, E. L., Faherty, J., et al. 2015, ApJ, 810, 158
Fischer, D. A., Marcy, G. W., & Spronck, J. F. P. 2014, ApJS, 210, 5
Follert, R., Dorn, R. J., Oliva, E., et al. 2014, Proc. SPIE, 9147, 914719
Foreman-Mackey, D., Hogg, D. W., Lang, D., & Goodman, J. 2013, PASP, 125, 306
Franson, K., Bowler, B. P., Zhou, Y., et al. 2023, ApJL, 950, L19
Gagné, J., Allers, K. N., Theissen, C. A., et al. 2018a, ApJL, 854, L27
Gagné, J., Faherty, J. K., Burgasser, A. J., et al. 2017, ApJL, 841, L1
Gagné, J., Mamajek, E. E., Malo, L., et al. 2018b, ApJ, 856, 23
Gaia Collaboration, Brown, A. G. A., Vallenari, A., et al. 2018, A&A, 616, A1
Gaia Collaboration, Brown, A. G. A., Vallenari, A., et al. 2021, A&A, 649, A1
Gaia Collaboration, Prusti, T., de Bruijne, J. H. J., et al. 2016, A&A, 595, A1
Gaia Collaboration, Vallenari, A., Brown, A. G. A., et al. 2023, A&A, 674, A1
Gao, P., Thorngren, D. P., Lee, E. K. H., et al. 2020, NatAs, 4, 951
Ginzburg, S., & Chiang, E. 2020, MNRAS, 491, L34
Gontcharov, G. A. 2006, AstL, 32, 759
Gonzales, E. C., Burningham, B., Faherty, J. K., et al. 2020, ApJ, 905, 46
Gonzales, E. C., Faherty, J. K., Gagné, J., Artigau, É., & Bardalez Gagliuffi, D. 2018, ApJ, 864, 100
Gray, D. F. 2008, The Observation and Analysis of Stellar Photospheres (3rd ed.; Cambridge: Cambridge Univ. Press)
Gray, R. O., Corbally, C. J., Garrison, R. F., McFadden, M. T., & Robinson, P. E. 2003, AJ, 126, 2048
Hargreaves, R. J., Gordon, I. E., Rey, M., et al. 2020, ApJS, 247, 55
Harris, C. R., Millman, K. J., van der Walt, S. J., et al. 2020, Natur, 585, 357
Hoch, K. K. W., Konopacky, Q. M., Theissen, C. A., et al. 2023, AJ, 166, 85
Holmberg, J., Nordström, B., & Andersen, J. 2009, A&A, 501, 941
Hood, C. E., Fortney, J. J., Line, M. R., & Faherty, J. K. 2023, ApJ, 953, 170
Horne, K. 1986, PASP, 98, 609
Howard, A. W., Marcy, G. W., Fischer, D. A., et al. 2014, ApJ, 794, 51
Hsu, C.-C., Burgasser, A. J., Theissen, C. A., et al. 2021, ApJS, 257, 45
Hsu, C.-C., Burgasser, A. J., & Theissen, C. A. 2023, ApJL, 945, L6
Hsu, C.-C., Burgasser, A. J., Theissen, C. A., et al. 2024, arXiv:2403.13760
Hsu, C.-C., Theissen, C., Burgasser, A., & Birky, J. 2021, SMART: The Spectral Modeling Analysis and RV Tool, v1.0.0, Zenodo, 10.5281/zenodo.4765258
Hunter, J. D. 2007, CSE, 9, 90
Husser, T.-O., Wende-von Berg, S., Dreizler, S., et al. 2013, A&A, 553, A6
Jeffreys, H. 1961, Theory of Probability. Oxford Classic Texts in the Physical Sciences (3rd ed.; Oxford: Oxford Univ. Press)
Kass, R. E., & Raftery, A. E. 1995, J. Am. Stat. Assoc., 90, 773
Kharchenko, N. V., Scholz, R. D., Piskunov, A. E., Röser, S., & Schilbach, E. 2007, AN, 328, 889
Kirkpatrick, J. D. 2005, ARA&A, 43, 195
Konopacky, Q. M., Baker, A. D., Mawet, D., et al. 2023, Proc. SPIE, 12680, 1268007
Konopacky, Q. M., Barman, T. S., Macintosh, B. A., & Marois, C. 2013, Sci, 339, 1398
Kotani, T., Kawahara, H., Ishizuka, M., et al. 2020, Proc. SPIE, 11448, 1144878
Kumar, S. S. 1962, AJ, 67, 579
Kumar, S. S. 1963, ApJ, 137, 1121
Landman, R., Stolker, T., Snellen, I., et al. 2024, A&A, 682, 48
Lavie, B., Mendonça, J. M., Mordasini, C., et al. 2017, AJ, 154, 91
López, R. A., Hoffman, E. B., Doppmann, G., et al. 2020, Proc. SPIE, 11447, 114476B
Luna, J. L., & Morley, C. V. 2021, ApJ, 920, 146
Macintosh, B., Graham, J. R., Barman, T., et al. 2015, Sci, 350, 64
Madhusudhan, N. 2012, ApJ, 758, 36
Mâlin, M., Boccaletti, A., Charnay, B., Kiefer, F., & Bézard, B. 2023, A&A, 671, A109
Mamajek, E. E., Bartlett, J. L., Seifahrt, A., et al. 2013, AJ, 146, 154
Marconi, A., Abreu, M., Adibekyan, V., et al. 2022, Proc. SPIE, 12184, 1218424
Marley, M., Saumon, D., Morley, C., & Fortney, J. 2018, Sonora 2018: Cloud-free, solar composition, solar C/O substellar evolution models v1.0, Zenodo, doi:10.5281/zenodo.2628068

Marley, M. S., Saumon, D., Visscher, C., et al. 2021, ApJ, 920, 85
Marois, C., Macintosh, B., Barman, T., et al. 2008, Sci, 322, 1348
Marsakov, V. A., & Shevelev, Y. G. 1995, BICDS, 47, 13
Martin, E. C., Fitzgerald, M. P., McLean, I. S., et al. 2018, Proc. SPIE, 10702, 107020A
Mawet, D., Bond, C. Z., Delorme, J. R., et al. 2018, Proc. SPIE, 10703, 1070306
Mawet, D., Delorme, J. R., Jovanovic, N., et al. 2017, Proc. SPIE, 10400, 1040029
Mawet, D., Fitzgerald, M. P., Konopacky, Q., et al. 2022, Proc. SPIE, 12184, 121841R
Mawet, D., Wizinowich, P., Dekany, R., et al. 2016, Proc. SPIE, 9909, 99090D
Mayor, M., & Queloz, D. 1995, Natur, 378, 355
McLean, I. S., Becklin, E. E., Bendiksen, O., et al. 1998, Proc. SPIE, 3354, 566
McLean, I. S., Graham, J. R., Becklin, E. E., et al. 2000, Proc. SPIE, 4008, 1048
Mesa, D., Gratton, R., Kervella, P., et al. 2023, A&A, 672, A93
Metchev, S. A., Heinze, A., Apai, D., et al. 2015, ApJ, 799, 154
Min, M., Hovenier, J. W., & de Koter, A. 2005, A&A, 432, 909
Min, M., Rab, C., Woitke, P., Dominik, C., & Ménard, F. 2016, A&A, 585, A13
Mishenina, T. V., Soubiran, C., Kovtyukh, V. V., & Korotin, S. A. 2004, A&A, 418, 551
Mollière, P., Molyarova, T., Bitsch, B., et al. 2022, ApJ, 934, 74
Mollière, P., Stolker, T., Lacour, S., et al. 2020, A&A, 640, A131
Mollière, P., Wardenier, J. P., van Boekel, R., et al. 2019, A&A, 627, A67
Nasedkin, E., Mollière, P., & Blain, D. 2024a, JOSS, 9, 5875
Nasedkin, E., Mollière, P., Lacour, S., et al. 2024b, arXiv:2404.03776
Nordström, B., Mayor, M., Andersen, J., et al. 2004, A&A, 418, 989
Nowak, G., Luque, R., Parviainen, H., et al. 2020, A&A, 642, A173
Öberg, K. I., Murray-Clay, R., & Bergin, E. A. 2011, ApJL, 743, L16
Otten, G. P. P. L., Vigan, A., Muslimov, E., et al. 2021, A&A, 646, A150
Patapis, P., Nasedkin, E., Cugno, G., et al. 2022, A&A, 658, A72
Pecaut, M. J., & Mamajek, E. E. 2013, ApJS, 208, 9
Perryman, M. A. C., Lindegren, L., Kovalevsky, J., et al. 1997, A&A, 323, L49
Petrus, S., Bonnefoy, M., Chauvin, G., et al. 2021, A&A, 648, A59
Popinchalk, M., Faherty, J. K., Kiman, R., et al. 2021, ApJ, 916, 77
Prato, L., Mace, G. N., Rice, E. L., et al. 2015, ApJ, 808, 12
Radigan, J., Jayawardhana, R., Lafrenière, D., et al. 2012, ApJ, 750, 105
Rice, M., & Brewer, J. M. 2020, ApJ, 898, 119
Rothman, L. S., Gordon, I. E., Barber, R. J., et al. 2010, JQSRT, 111, 2139
Ruffio, J.-B., Horstman, K., Mawet, D., et al. 2023, AJ, 165, 113
Ruffio, J.-B., Konopacky, Q. M., Barman, T., et al. 2021, AJ, 162, 290
Ruffio, J.-B., Macintosh, B., Konopacky, Q. M., et al. 2019, AJ, 158, 200
Schneider, A. C., Burgasser, A. J., Bruursema, J., et al. 2023, ApJL, 943, L16
Serabyn, E., Huby, E., Matthews, K., et al. 2017, AJ, 153, 43
Skilling, J. 2004, in ASP Conf. Ser. 735, 24th International Workshop on Bayesian Inference and Maximum Entropy Methods in Science and Engineering, ed. R. Fischer, R. Preuss, & U. V. Toussaint (San Francisco, CA: AIP), 395
Skilling, J. 2006, BayAn, 1, 833
Soubiran, C., Le Campion, J.-F., Brouillet, N., & Chemin, L. 2016, A&A, 591, A118
Soubiran, C., Le Campion, J. F., Cayrel de Strobel, G., & Caillo, A. 2010, A&A, 515, A111
Speagle, J. S. 2020, MNRAS, 493, 3132
Stassun, K. G., Oelkers, R. J., Paegert, M., et al. 2019, AJ, 158, 138
Suchkov, A. A., Makarov, V. V., & Voges, W. 2003, ApJ, 595, 1206
Tannock, M. E., Metchev, S., Heinze, A., et al. 2021, AJ, 161, 224
Taylor, B. J. 2005, ApJS, 161, 444
Theissen, C. A., Konopacky, Q. M., Lu, J. R., et al. 2022, ApJ, 926, 141
Trujillo, I., Aguerri, J. A. L., Cepa, J., & Gutiérrez, C. M. 2001, MNRAS, 328, 977
Tsantaki, M., Pancino, E., Marrese, P., et al. 2022, A&A, 659, A95
Valenti, J. A., & Fischer, D. A. 2005, ApJS, 159, 141
van Dam, M. A., Bouchez, A. H., Le Mignant, D., et al. 2006, PASP, 118, 310
van Leeuwen, F. 2007, A&A, 474, 653
van Leeuwen, F., Evans, D. W., Grenon, M., et al. 1997, A&A, 323, L61
Vargas Catalán, E., Huby, E., Forsberg, P., et al. 2016, A&A, 595, A127
Vigan, A., El Morsy, M., Lopez, M., et al. 2024, A&A, 682, 16
Virtanen, P., Gommers, R., Oliphant, T. E., et al. 2020, NatMe, 17, 261
Vos, J. M., Allers, K. N., & Biller, B. A. 2017, ApJ, 842, 78
Vos, J. M., Allers, K. N., Biller, B. A., et al. 2018, MNRAS, 474, 1041
Vos, J. M., Biller, B. A., Bonavita, M., et al. 2019, MNRAS, 483, 480
Vos, J. M., Faherty, J. K., Gagné, J., et al. 2022, ApJ, 924, 68,
Wang, J., Kolecki, J. R., Ruffio, J.-B., et al. 2022, AJ, 163, 189
Wang, J., Wang, J. J., Ruffio, J.-B., et al. 2023, AJ, 165, 4
Wang, J. J., Ruffio, J.-B., Morris, E., et al. 2021, AJ, 162, 148
Waskom, M. L. 2021, JOSS, 6, 3021
Whiteford, N., Glasse, A., Chubb, K. L., et al. 2023, MNRAS, 525, 1375
Wilcomb, K. K., Konopacky, Q. M., Barman, T. S., et al. 2020, AJ, 160, 207
Wizinowich, P. L., Le Mignant, D., Bouchez, A. H., et al. 2006, PASP, 118, 297
Xin, Y., Xuan, J. W., Mawet, D., et al. 2023, JATIS, 9, 035001
Xuan, J. W., Bryan, M. L., Knutson, H. A., et al. 2020, AJ, 159, 97
Xuan, J. W., Wang, J., Finnerty, L., et al. 2024, ApJ, 962, 10
Xuan, J. W., Wang, J., Ruffio, J.-B., et al. 2022, ApJ, 937, 54
Zahnle, K. J., & Marley, M. S. 2014, ApJ, 797, 41
Zapatero Osorio, M. R., Martín, E. L., Bouy, H., et al. 2006, ApJ, 647, 1405
Zhang, Z., Mollière, P., Hawkins, K., et al. 2023, AJ, 166, 198,
Zhou, T., Jacobsen, D., Vazquez-Segovia, B., et al. 2023, RNAAS, 7, 50
Zuckerman, B., Rhee, J. H., Song, I., & Bessell, M. S. 2011, ApJ, 732, 61